

The velocity modulation of galaxy properties in and near clusters: quantifying the decrease in star formation in backplash galaxies

Smriti Mahajan^{1*}, Gary A. Mamon^{2,3} and Somak Raychaudhury¹

1: School of Physics and Astronomy, University of Birmingham, Birmingham B15 2TT, United Kingdom

2: Institut d'Astrophysique de Paris (IAP), 98-bis Blvd Arago, F-75014 Paris, France

3: Astrophysics & BIPAC, Department of Physics, University of Oxford, Keble Rd, Oxford OX1 3RH, United Kingdom

ABSTRACT

The efficiency of ongoing/recent star formation in galaxies is known to decrease with increasing projected distance from the centre of a cluster out to several times its virial radius (R_v). Using a complete sample ($M_r \leq -20.5$, $0.02 \leq z \leq 0.15$) of galaxies in and around 268 clusters from the SDSS DR4, we investigate how, at a given projected radius from the cluster centre, the stellar mass and star formation properties of a galaxy depend on its absolute line-of-sight velocity in the cluster rest frame, $|v_{\text{LOS}}|$. We find that for projected radii $R < 0.5 R_v$, the fraction of high mass non-BCG galaxies increases towards the centre for low $|v_{\text{LOS}}|$, which may be the consequence of the faster orbital decay of massive galaxies by dynamical friction. At a given projected radius, the fraction of Galaxies with Ongoing or Recent ($< 1-3$ Gyr) Efficient Star Formation (GORES, with $\text{EW}(\text{H}\delta) > 2 \text{ \AA}$ & $\text{D}_n4000 > 1.5$) is slightly but significantly lower for low $|v_{\text{LOS}}|$ galaxies than for their high velocity counterparts. We study these observational trends with the help of a dark matter (DM) cosmological simulation. We classify DM particles as virial, infall, and backplash according to their present positions in (r, v_r) radial phase space and measure the frequencies of each class in cells of $(R, |v_{\text{LOS}}|)$ projected phase space. As expected, the virial class dominates at projected radii $R < R_v$, while the infall particles dominate outside, especially at high $|v_{\text{LOS}}|$. However, the backplash particles account for at least one-third (half) of all particles at projected radii slightly greater than the virial radius and $|v_{\text{LOS}}| < \sigma_v$ ($|v_{\text{LOS}}| \ll \sigma_v$). The deprojection of the GORES fraction leads to a saturated linear increase with radius. We fit simple models of the fraction of GORES as a function of class only or class and distance to the cluster centre (as in our deprojected fraction). While GORES account for $18 \pm 1\%$ of all galaxies within the virial cylinder, in our best-fit model, they account for $13 \pm 1\%$ of galaxies within the virial sphere, $11 \pm 1\%$ of the virial population, $34 \pm 1\%$ of the distant (for projected radii $R < 2 R_v$) infall population and $19 \pm 4\%$ of the backplash galaxies. Also, $44 \pm 2\%$ of the GORES within the virial cylinder are outside the virial sphere. These fractions are very robust to the precise good-fitting model and to our scheme for assigning simulation particle classes according to their positions in radial phase space (except for two of our models, where the fraction of GORES reaches $27 \pm 4\%$). Given the 1–3 Gyr lookback time of our GORES indicators, these results suggest that star formation in a galaxy is almost completely quenched in a single passage through the cluster.

Key words: Galaxies: clusters: general; galaxies: evolution; galaxies: starburst; galaxies: star formation; galaxies: kinematics and dynamics

1 INTRODUCTION

The wide variety in star formation properties of galaxies is an inevitable consequence of the varied environments they inhabit. Physical properties of galaxies such as morphology (Dressler 1980), colour (e.g. Balogh et al. 2004b), luminosity (e.g. Adami, Biviano, & Mazure 1998), individual spectral indices used as star formation rate (SFR) tracers, such as the equivalent width

(EW) of [OII] or $\text{H}\alpha$ (e.g. Balogh et al. 2004a; Haines et al. 2006), are known to vary systematically with environment. As they leave their sparsely populated base in the *field* for the high density regions of galaxy clusters, galaxies see their dominant stellar population become older, emission lines disappear from their spectra, complex spirals are transformed into more uniform spheroids, and the SFR decreases by 1–2 orders of magnitude.

It is thus generally believed that the cluster environment is hostile to star formation. For example, the denser the environment, the stronger will be the stripping of interstellar gas either

* E-mail: sm@star.sr.bham.ac.uk

by the ram pressure of the intra-cluster gas (Gunn & Gott 1972) or by the tidal field of the cluster (Merritt 1983), leading to star-formation for subsequent star formation (Larson, Tinsley, & Caldwell 1980). So a galaxy that entered the cluster virial radius ~ 1 Gyr ago, and has since crossed the core of the cluster, should have lost its gas via either of these two effects during its passage through the cluster core (see for instance Vollmer 2009 for the impact of ram-pressure stripping in the Virgo cluster). Moreover, in the intermediate density environments on the cluster outskirts, mechanisms like galaxy-galaxy interactions (e.g. Moore et al. 1996) seem to dominate the process of galaxy evolution (e.g. Porter & Raychaudhury 2007; Porter et al. 2008; Mahajan, Raychaudhury, & Pimbblet 2011). Thus star-forming *in-falling* galaxies are expected to have distinctive properties compared to the passively evolving *virialised* population inside the cluster.

However, one can define an intermediate population of galaxies that have travelled through the cluster core (perhaps more than once) and have not yet had time to mix with the virialised population. These *backsplash*¹ galaxies would have felt the first effects of the cluster environment, but may not have evolved all the way to attain the passive properties of the virialised population. In their simulations of six clusters, Balogh, Navarro, & Morris (2000) find that $54\% \pm 20\%$ of dark matter (DM) particles at $1 - 2 R_{200}$ from the cluster centre have been inside the virial radius (R_{200}) from an earlier time. Gill et al. (2005) estimate similar fractions, considering a virial radius equivalent to R_{100} , and further add that 90% of such particles go as close to the cluster centre as 50% of the virial radius. Mamon et al. (2004) used both analytical methods and cosmological simulations to conclude that DM particles travel through the core of the cluster out to $1 - 2.5 R_{100}$ on the other side.

The backsplash galaxies may contribute to the observation that the radial trends of star formation diagnostics extend to at least twice the virial radius (Balogh et al. 2000) from cluster centres. Hence, the intermediate environments found in inter-cluster filaments and on the outskirts of galaxy clusters play a key role in defining the evolutionary history of galaxies (Rines et al. 2003; Gill et al. 2005; Porter & Raychaudhury 2007; Porter et al. 2008; Mahajan et al. 2010, 2011).

Most results indicate that the properties of galaxies evolve as they encounter denser environments, i.e. progress from the field towards the cluster. This could be due to the prevalence of smaller clusters (galaxy groups) as one approaches rich clusters, as the tidal field and possibly some mild form of ram pressure stripping might play a similar role, as they do in more massive clusters, to deplete the gas reservoirs of galaxies. Alternatively, it is possible that the gas reserves of galaxies may be protected by the pressure of the surrounding intra-group medium (IGM) from being tidally perturbed, preventing the star formation in the galaxy from being quenched, even after spending > 1 Gyr in crossing the cluster. In such a case, an increase in tides generated during the group-cluster merger may instead result in an enhancement of the SFR of group galaxies (Bekki 1999). Although such a group pre-processing scenario is yet to be confirmed, some evidence in its favour is found in recent observational studies (e.g. Oemler et al. 2009).

The main difference between the infalling and backsplash galaxies is that the former have larger apocentres, hence larger radial (3D) velocities. Hence, one expects that the backsplash galax-

ies will have lower absolute line-of-sight (hereafter, LOS) velocities² than the infalling galaxies. One is therefore motivated to study the modulation of the radial trends of galaxy properties, with absolute LOS velocity.

In the central regions of clusters, the relative velocities of galaxies have been found to be correlated with their luminosity (e.g. Chincarini & Rood 1977; Struble 1979; Bothun & Schombert 1990; Biviano et al. 1992), morphology (de Vaucouleurs 1961; Sandage & Tammann 1976; Moss & Dickens 1977; Helou et al. 1979; Sodre et al. 1989; Biviano et al. 1992; Girardi et al. 2003, among others), and more recently spectral type (Biviano et al. 1997; Pimbblet et al. 2006). The early-type, massive and passive galaxies are found to have lower velocity dispersion relative to their late-type, star-forming counterparts. It has been shown that this velocity segregation of mass (or luminosity) in cluster galaxies is neither induced by morphological segregation nor limited to cD galaxies (Biviano et al. 1992).

There have been some efforts to study the velocity segregation in galaxy properties on the outskirts of galaxy clusters (e.g. Mohr et al. 1996; Rines et al. 2005; Pimbblet et al. 2006). In particular, Rines et al. (2005) found no significant difference in the velocity distribution of the emission-line and absorption-line galaxies with projected radii between 1 and $2 R_{200}$ in a sample of eight nearby x-ray bright clusters. However, emission-line galaxies outside the virial radius appear to have a significantly larger velocity dispersion than their absorption-line counterparts (but Rines et al. do not provide any quantitative estimate of the significance). Moreover, from fig. 6 of Rines et al., the mean velocity dispersion profile of emission-line galaxies appears significantly steeper than that of non-emission-line galaxies (this trend was not noted by the authors). Rines et al. concluded that star-forming galaxies in the infall regions are not field interlopers, which lead them to reject a simple model where the truncation of star formation at low projected radius was solely caused by the efficient quenching of star formation in (backsplash) galaxies that have crossed through the cluster.

In this paper, using the very large Sloan Digital Sky Survey (SDSS), we have collected sufficient data around hundreds of clusters to analyse the differences in the distribution in *projected phase space* (projected radius R and absolute LOS velocity $|v_{\text{LOS}}|$) of star-forming and passive galaxies at much finer resolution than previously performed. We look for and find a significant velocity modulation of the variations in stellar mass and star-formation properties with projected radius. We also build simple dynamical models involving the virial, infalling and backsplash populations of galaxies to explain our results, calibrating our models and the projection effects using a cosmological simulation.

The organisation of this paper is as follows: in the following section we describe the observational dataset and briefly describe our star formation diagnostics. In §3 we present the analysis of the SDSS galaxies around clusters, focusing on the velocity modulation of radial trends in stellar mass and star formation efficiency. In §4 we model our results using a cosmological simulation described in §4.1 to classify particles into virial, infall and backsplash populations (§4.2). In §4.3, we fit simple models of the variation with physical radius of the fraction of *Galaxies with Ongoing or Recent Efficient Star formation* (hereafter, GORES) for each of the three populations to the observed fraction of GORES as a function of projected radius and LOS velocity. We discuss and summarise our results and their implications in §5. Throughout this paper we

¹ The term *backsplash galaxies* was first coined by Gill, Knebe, & Gibson (2005).

² Our absolute LOS velocities are in the cluster frame.

assume a concordance cosmology with $\Omega_m = 0.3$, $\Omega_\Lambda = 0.7$, and $h = 0.7$.

2 DATA

2.1 The cluster catalogue

We selected our galaxy clusters from the ‘group’ catalogue compiled by Yang et al. (2007) from the Fourth Data Release (DR4) of the SDSS. Their iterative algorithm identifies first order groups using a Friends-of-Friends (FoF) algorithm in redshift space, with a small linking length in projected space and a large one along the direction of the LOS. This algorithm thus selects potential groups at a high surface density threshold, so that groups embedded within the virial radii of more massive ones will be extracted as two (or more) separate entities. All galaxies left out by this grouping method are treated as additional potential groups (of single galaxies).

The raw luminosities and (luminosity-weighted) centres of the clusters are measured and then the luminosities (corrected for incompleteness), masses (assuming a given mass-to-light ratio) and velocity dispersions (from a mass / velocity dispersion relation) are derived. The radii R_{180} , i.e. of spheres that are 180 times denser than the critical density of the Universe are derived from the masses. The distribution of galaxies around each group centre in projected phase space are examined to determine group membership, based upon the assumption of a projected Navarro, Frenk, & White (1996, hereafter NFW) surface density profile and a Gaussian distribution of LOS velocities with dispersion independent of projected radius. The algorithm is iterated with these new group assignments, where the mass-to-light ratio used for estimating the new mass is a function of luminosity derived from the previous iteration. The iteration continues until the membership converges. Yang et al. (2007) have tested their algorithm on mock galaxy catalogues constructed in real space and converted to redshift space.

In the present work, we define the galaxy clusters with the following criteria:

- (i) redshift range: $0.02 \leq z \leq 0.12$;
- (ii) membership: at least 15 galaxies;
- (iii) minimum halo mass (within R_{180}): $10^{14} M_\odot$.

All of our chosen clusters have at least 12 galaxies ($M_r \leq -20.5$) with SDSS spectra within R_{180} of each cluster centre. For our chosen cosmology, the virial radius, within which the cluster may be thought to be in dynamical equilibrium, is commonly believed to be very close to R_{100} where the density is 100 times critical. In this paper, we adopt R_{100} for the virial radius, and more precisely

$$R_v = 1.3 R_{180}, \quad (1)$$

which, for NFW models with concentrations between 3 and 10, matches R_{100} to an accuracy of 2%. This gives us a sample of 268 clusters in the SDSS DR4 footprint with median $M_{180} \sim 10^{14.2} M_\odot$, corresponding to a median virial radius $R_{100} = 1.5$ Mpc (using Eq. 1).

The range of 1.5 dex in cluster masses should not be a concern given that the properties of non-central (satellite) galaxies depend little on the mass of the group or cluster they live in (van den Bosch et al. 2008).

2.2 Galaxy data

The observed photometric and spectroscopic data for galaxies in this work are taken from the SDSS DR4 (Adelman-McCarthy & the SDSS collaboration 2006). We use the galaxy magnitudes, k -corrections and the corresponding galactic extinction values in the SDSS g and r -bands from the New York University Value Added Galaxy Catalogue (NYU-VAGC; Blanton et al. 2005). We k -correct these magnitudes to $z = 0.1$, which is the median redshift of the sample. We select galaxies that meet the following criteria:

- (i) redshift range $0.02 \leq z \leq 0.15$;
- (ii) absolute magnitude: $M_r \leq -20.5$;
- (iii) half-light angular radius: $\theta_{\text{eff}} \leq 5''$;
- (iv) projected separation with cluster: $R < 2 R_v$;
- (v) velocity relative to cluster: $|v_{\text{LOS}} - v_{\text{LOS}}^{\text{cluster}}| \leq 3 \sigma_v^{\text{cluster}}$.

Our luminosity limit roughly corresponds to $L \geq 0.5 L_*$ (given that $M_{r,*}^{0.1} = -20.44 + 5 \log h$, Blanton et al. 2003), which corresponds to the apparent magnitude limit ($r \leq 17.77$) for the SDSS spectroscopic catalogue at $z = 0.1$. Our galaxy redshifts are chosen in an interval that is slightly larger than for the clusters, so as to avoid missing galaxies lying behind (or in front) of the most (least) distant clusters. The angular size criterion ensures that the spectrum obtained from the $3''$ SDSS fibre is a fair representation of the light from the galaxy, and does not just correspond to the passive central bulge of the galaxy.

This gives us a sample of 19,904 galaxies in or near 268 clusters covered out to 2 virial radii in projection and 3 times the cluster velocity dispersions along the LOS.

The cluster galaxies are compared with a sample of 21,100 field galaxies, randomly chosen to have the same redshift and luminosity distributions as those of the cluster galaxies. We require the field galaxies to lie at least 10 Mpc away from the centres of all groups with $N \geq 5$ and halo mass $\geq 10^{12.5} M_\odot$ in the Yang et al. (2007) catalogue (this includes clusters). Since the galaxy properties depend on their distance from the nearest large structure (e.g. Mahajan et al. 2011) out to $\sim 3 R_{200}$ ($\lesssim 6 h_{70}^{-1}$ Mpc; e.g. Rines et al. 2003; Mahajan et al. 2011), a linear distance of 10 Mpc (corresponding to typically $6.7 R_v$) from all groups and clusters ensures that our field sample is not contaminated by the effect of any groups or clusters.

2.3 Star formation diagnostics

In this paper, as our principal diagnostic, we use the specific star formation rate (SFR/ M^*) of a galaxy, as estimated from the optical spectrum, by Brinchmann et al. (2004) for all galaxies belonging to the spectroscopic catalogue of SDSS DR4. From this and a few other spectral indices, namely the emission-corrected $H\delta_A$ (hereafter, $H\delta$) EW and the 4000 Å break, estimated in a related work (Kauffmann et al. 2003), we compare the trends seen in the current star formation activity and star formation histories (SFHs) of different types of galaxies.

Brinchmann et al. have constructed a model grid of $\sim 2 \times 10^5$ spectral synthesis models (Bruzual & Charlot 1993; Charlot & Longhetti 2001) over four main parameters spanning a range of $-1 < \log Z/Z_\odot < 0.6$ in metallicity (Z), $-4.0 < \log U < -2.0$ in ionisation parameter (U), $0.01 < \tau_V < 4.0$ in total dust extinction (τ_V) and $0.1 < \xi < 0.5$ in dust-to-metal ratio (ξ). Dust attenuation is also treated with a very sophisticated model of Charlot & Fall (2000), which provides a consistent model for ul-

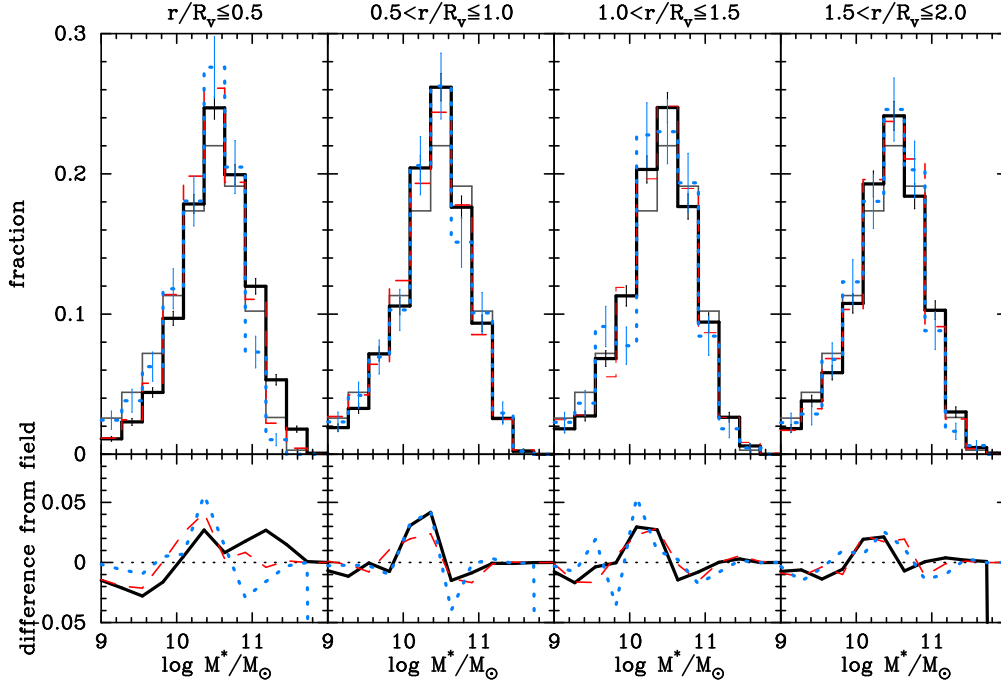


Figure 1. The distribution of stellar masses for our galaxy samples, in four bins of projected radius in the four panels from left to right. The *solid black*, *dashed red* and *dotted blue* distributions represent absolute LOS velocity bins $|v_{\text{LOS}}|/\sigma_v = 0-1$, $1-2$ and $2-3$ respectively. The *thin grey* distribution denotes the field. The *bottom panels* show the difference between the binned cluster distributions and that of the field. The *error bars* are Poisson. In the flux limited SDSS, galaxies in the local Universe have their M^* distribution centred around $M^* = 3 \times 10^{10} M_\odot$ (Kauffmann et al. 2003). A significant fraction of galaxies with $M^* \geq 10^{11} M_\odot$ are found only in the core of galaxy clusters. Interestingly, the low absolute LOS velocity galaxies in the cores are the ones which are more massive, while the high velocity galaxies mostly inhabit the low mass end.

traviolet (UV) to infrared (IR) emission. They then go on to derive the values for the SFR and SFR/M^* using a Bayesian technique, considering the entire spectrum of each galaxy. The derived parameters (SFR and SFR/M^*) are then corrected for aperture biases using photometric colours. Their analysis of line ratios is insensitive to stellar ages, SFH and the relative attenuation by dust in the gas clouds and the interstellar medium. Out of the three statistical estimates (mean, median & mode) for the probability distribution function of SFR/M^* derived for each galaxy, we used the median of the distribution in this paper, since it is independent of binning.

The spectrum of a galaxy that has experienced a burst of star formation in the recent past (1–3 Gyr ago) is expected to show a strong absorption of $\text{H}\delta$ in the optical spectrum. This is because A type stars, which significantly contribute to the $\text{H}\delta$ absorption, have a lifetime of $\lesssim 1.5$ Gyr, but a burst of star formation can produce enough ionising radiation to fill in the $\text{H}\delta$ absorption. However, as the episode of star formation ends, the $\text{H}\delta$ absorption line becomes more transparent. The $\text{EW}(\text{H}\delta)$ has been extensively used in the literature to measure the mean stellar age of galaxies, and the elapsed time since the last major burst (e.g. Worthey & Ottaviani 1997; Kauffmann et al. 2003). At the other extreme is the 4000 Å break (D_n4000), which is the strongest discontinuity occurring in the optical spectrum of a galaxy, from the accumulation of absorption lines of mainly ionised metals. As the opacity increases with decreasing stellar temperature, the value of D_n4000 is largest for old and metal-rich stellar populations. Stellar population synthesis models indicate that D_n4000 is mostly sensitive to age, except for sub-solar metallicity populations older than 1 Gyr, where it is also strongly dependent on metallicity (Kauffmann et al. 2003).

Interestingly, the variation of $\text{H}\delta$ with D_n4000 is not sensi-

tive to metallicity or dust extinction, thus providing a good measure of SFH, such that for a given D_n4000 , stronger $\text{H}\delta$ implies that the galaxy has experienced a recent burst in star formation (Kauffmann et al. 2003). In particular, the right panel of Kauffmann et al.’s fig. 2 indicates that the combination of $\text{H}\delta > 2 \text{ \AA}$ and $D_n4000 < 1.5$ leads to stellar populations younger than 1 to 3 Gyr for solar and 0.2 solar metallicity populations, respectively.

3 VELOCITY MODULATION OF GALAXY PROPERTIES

The key issue that we are trying to address in this paper is whether it is possible to distinguish the galaxies that have passed through the cluster core from those that are falling into it for the first time, based on observable parameters. DM simulations show that the backplash population is most likely to be seen between $1 - 1.5R_v$ and with velocities lower than the mean velocity of the cluster (e.g. Mamon et al. 2004; Gill et al. 2005). So, we stack together all the galaxies found in clusters within $2R_v$ and $|\Delta v_{\text{LOS}}| < 3\sigma_v$, into four bins of projected radius of width $0.5R_v$, and into three bins of absolute LOS velocity: $|\Delta v_{\text{LOS}}|/\sigma_v < 1$, $1-2$ and $2-3$ respectively. Below we describe the features of these distributions for various galaxy properties with respect to one another and the field distribution.

3.1 Stellar mass

In Fig. 1 we plot the distribution of stellar masses for the 12 classes (3 scaled velocity bins in each of the 4 scaled radial bins) of galax-

ies as described above. Due to the flux limit of SDSS, the stellar mass distribution of galaxies in Fig. 1 appears to be centred around $M^* = 3 \times 10^{10} M_\odot$ in the local Universe (also see Kauffmann et al. 2003). The most massive galaxies ($\log M^*/M_\odot \geq 11$) are mostly confined to the cores of the clusters. However, even in the core there seems to be a correlation between the relative LOS velocity of a galaxy with respect to the cluster and its stellar mass. The Kolmogorov-Smirnov³ (K-S henceforth) statistics show that the most massive galaxies in clusters have low velocities with respect to the cluster, and the high velocity galaxies show an affinity for the field distribution, which is skewed towards the low mass end. The detailed statistical comparison between different distributions is shown in Table A1 in Appendix.

When the brightest cluster galaxies (BCGs) are excluded, there is no mass segregation in clusters relative to the field (von der Linden et al. 2010). To explore the inter-dependence of M^* , R_v and LOS velocity of galaxies in clusters, we repeated our analysis by excluding the BCGs from the clusters. Contrary to von der Linden et al. (2010), we find that the different distributions still show similar trends: in the inner regions of clusters the most massive galaxies have lowest absolute LOS velocities (see Table A2).

To analyse mass segregation in a different way, in Fig. 2 we show the fraction of high-stellar mass galaxies as a function of projected radius in three bins of absolute LOS velocity, discarding BCGs. Fig. 2 confirms our impression that *mass segregation is present, but only at $R < 0.5 R_v$, and only for the low- and intermediate $|v_{\text{LOS}}|$ galaxies.*

The difference in low and high mass velocity distributions in the projected cluster core is not simply caused by the BCGs, which are excluded from Fig. 2 (see also Table A2). While Biviano et al. (1992) also found that high mass non-BCG galaxies had lower absolute LOS velocities, we find that this is limited to galaxies within $0.5 R_v$. In other words, we find that *the high absolute LOS velocity galaxies show no mass segregation*, in contrast with the global luminosity segregation found by others (e.g. Adami et al. 1998; von der Linden et al. 2010), when no cuts are made on absolute LOS velocity (which we also find, since the high absolute LOS velocity galaxies are much rarer than their intermediate and low velocity counterparts). We discuss mass segregation amongst cluster galaxies further in §5.1.

3.2 Galaxy colours

Broadband photometric colours are widely used as proxies for the star formation activity of galaxies. In this paper, we use the ‘colour offset’, which is the difference between the $(g-r)^{0.1}$ (extinction-corrected) colour of a galaxy and that of the red sequence for a galaxy of the same magnitude, where the red sequence is fitted by stacking all the cluster galaxies together. In Fig. 3 we plot the distribution of the colour offset for all 12 classes of galaxies.

The low velocity galaxies in cluster cores are found to have the reddest colours, indicative of their passive evolution. But interestingly, even within the cores, the difference between the colours of high and low velocity galaxies indicates statistically significant different distributions (see Table A3). Out to $2 R_v$, the distribution

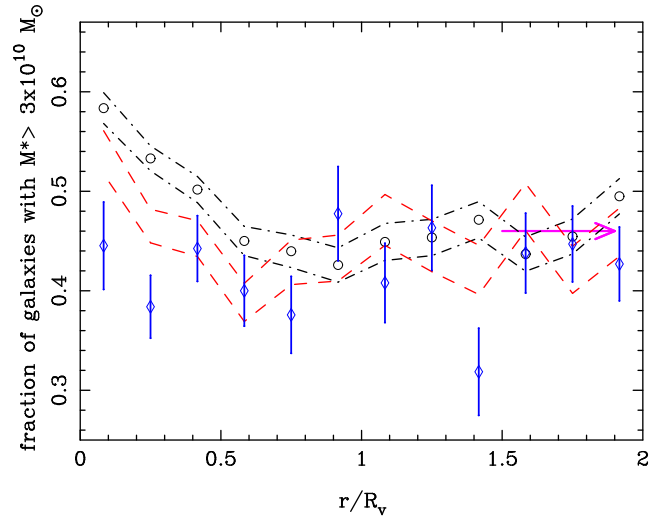


Figure 2. The fraction of high stellar mass galaxies ($M^* \geq 3 \times 10^{10} M_\odot$, with brightest cluster galaxies removed), plotted as a function of scaled radius from the cluster centre. The low ($0 - 1 \sigma_v$) and high ($> 2 \sigma_v$) absolute velocities (shown as black circles and blue diamonds respectively), and the $\pm 1 \sigma$ range (from binomial statistics) are shown as black dash-dotted lines, red dashed lines, and blue error bars, for the low, intermediate ($1 - 2 \sigma_v$) and high LOS absolute velocities, respectively. The magenta arrow indicates the field value.

of the colour offset for the field galaxies is very different from that of the galaxies residing in and around clusters. This might suggest that the broadband colours could be very easily modulated by slight changes in the local and/or global environment, and are hence not very well suited for the study of evolutionary trends amongst galaxies (see also Mahajan, Haines, & Raychaudhury 2010; Mahajan, Raychaudhury, & Pimbblet 2011). As discussed below, on the outskirts of clusters ($1 - 1.5 R_v$) the trends seen for broadband colours are consistent with those seen for spectroscopic parameters.

3.3 Diagnostics of specific star formation rate and star formation history

It has been shown that the SFR of galaxies is a function of their stellar mass (e.g. Noeske et al. 2007b). So in this work we prefer to use the specific star formation rate (SFR/M^*) to quantify the *current* star formation activity in a galaxy. In Fig. 4, we plot the distributions of SFR/M^* , as estimated by Brinchmann et al. (2004), for all the galaxies in the spectroscopic galaxy catalogue of the SDSS DR4.

As expected, the cluster galaxies within $0.5 R_v$ have their $\log \text{SFR}/M^*$ distributions heavily skewed towards the lower end, indicating passive evolution. Interestingly though, the high end of the values of SFR/M^* in the cluster core, and almost at all radii out to $1.5 R_v$, mostly belongs to galaxies with high velocities. K-S statistics show the difference between the lowest and the highest velocity galaxy distributions to be statistically significant in the core ($< 0.5 R_v$) and on the cluster outskirts ($1 - 1.5 R_v$; see Table A4). The field distribution is significantly different from all other classes of galaxies, becoming indistinguishable from the high velocity galaxies only in the outermost radial bin.

³ The null hypothesis for the K-S test is that both the distributions being compared are drawn from the same parent distribution, i.e. if the two distributions are identical, the probability (p) of the null hypothesis being satisfied is unity.

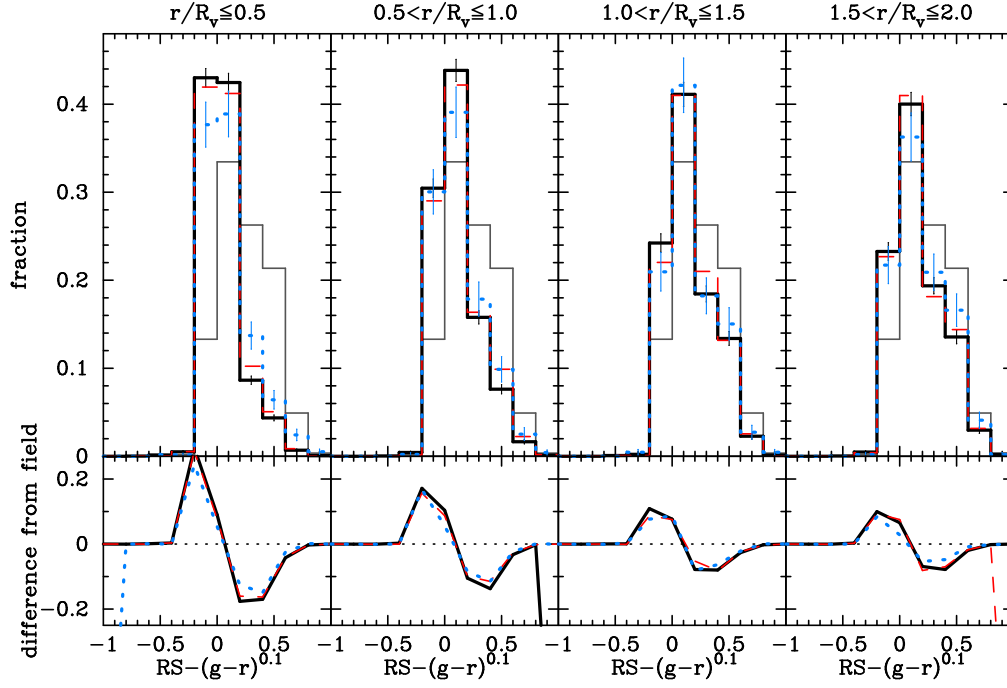


Figure 3. Same as Fig. 1 but for the “colour offset” of cluster galaxies, i.e., the difference between the $(g-r)^{0.1}$ colour of a galaxy and the Red Sequence colour for a galaxy of the same magnitude. Galaxies bluer than the fitted red sequence (see text) have positive values of the offset on the x-axis. The build-up of the blue tail of the distribution outwards from the cluster core is clearly seen. Interestingly, even in the outermost radial bin ($1.5-2R_v$), there are more red sequence galaxies than the field. This shows that physical processes, dependent on environment, efficiently modify properties of galaxies in regions with densities in between the two extremes characterising cluster cores and the field.

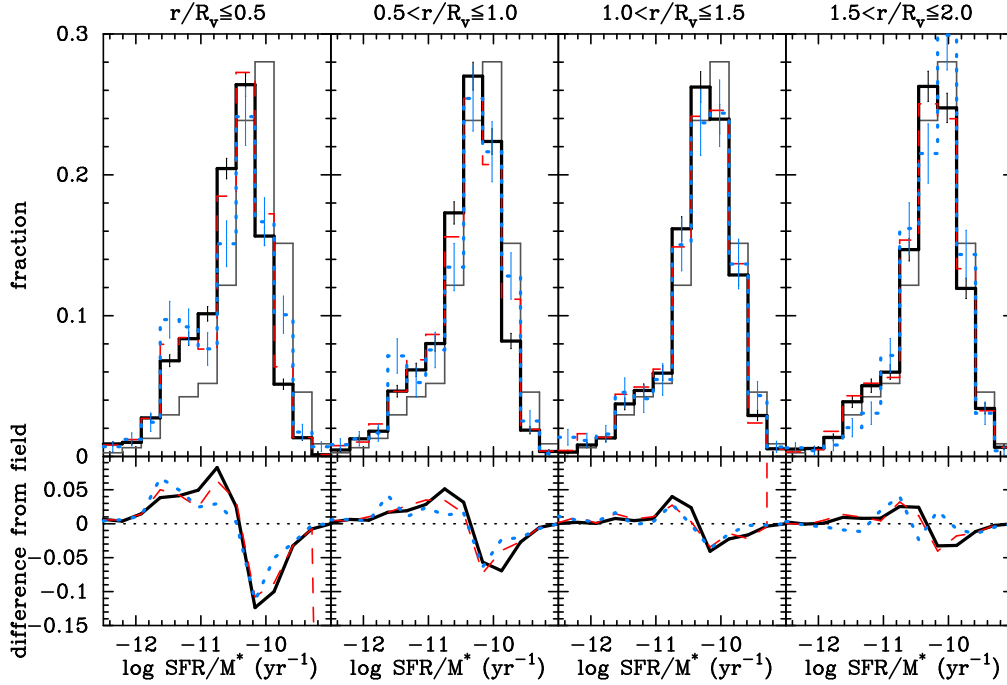


Figure 4. Same as Fig. 1 but for SFR/M^* . As expected, the cluster distributions are skewed towards the low $\log SFR/M^*$ end in the core region, but only a small tail of galaxies with low $\log SFR/M^*$ is seen in the outer radial bins.

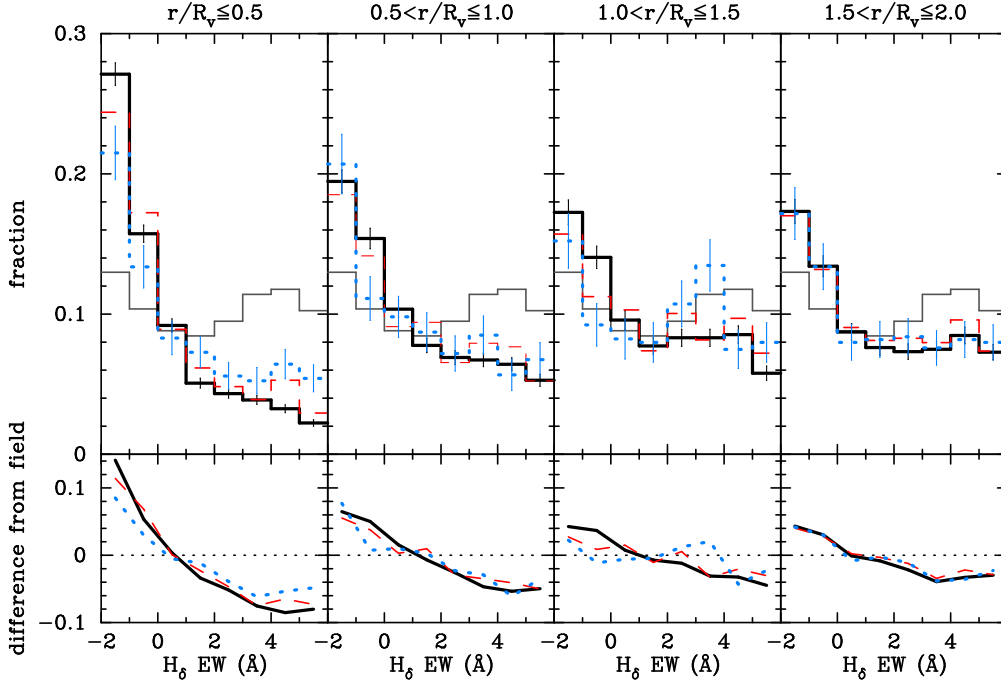


Figure 5. Same as Fig. 1 but for D_n4000 . The field distribution is bimodal with a minimum at $D_n4000 \sim 1.5$. The passively evolving galaxies in the cluster core are old and metal-rich, hence their distribution peaks at the high end of the D_n4000 . However, the high velocity galaxies in the cluster core (dotted blue line) have a distribution similar to that of field galaxies. The trend continues out to $1.5 R_v$, beyond which the distributions almost merge with the field. The K-S statistics show the distributions of the high and low velocity galaxies to be statistically different at all radial distances within $1.5 R_v$.

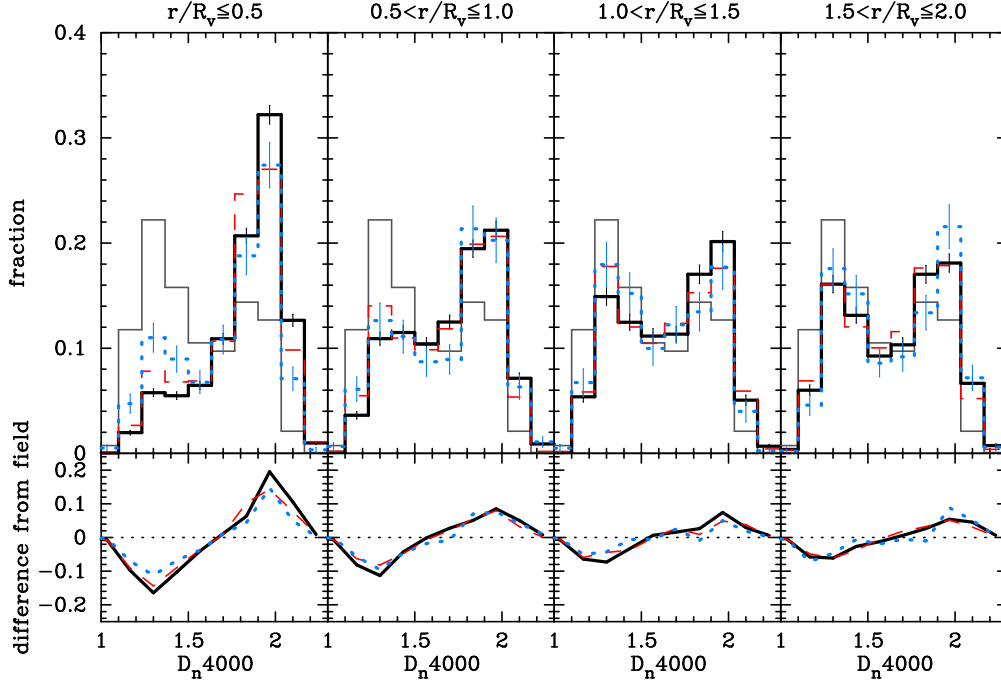


Figure 6. Same as Fig. 1 but for $EW(H\delta)$. This plot complements the results in Fig. 5. The field distribution shows a clear bimodality around 2 \AA . The galaxies in the core of the cluster, most of which are evolving passively, do not show absorption in $H\delta$. It is interesting to note that the high velocity galaxies in the innermost bins, which are likely to be the newest entrants in the core, are also the ones which are most likely to have experienced a burst of star formation as indicated by relatively high $EW(H\delta)$. This trend in velocity classes continues out to $2 R_v$, where the difference between the field and the low velocity galaxies is minimum. The difference between the highest (blue) and the lowest velocity (black) galaxies is statistically significant in all radial bins out to $1.5 R_v$.

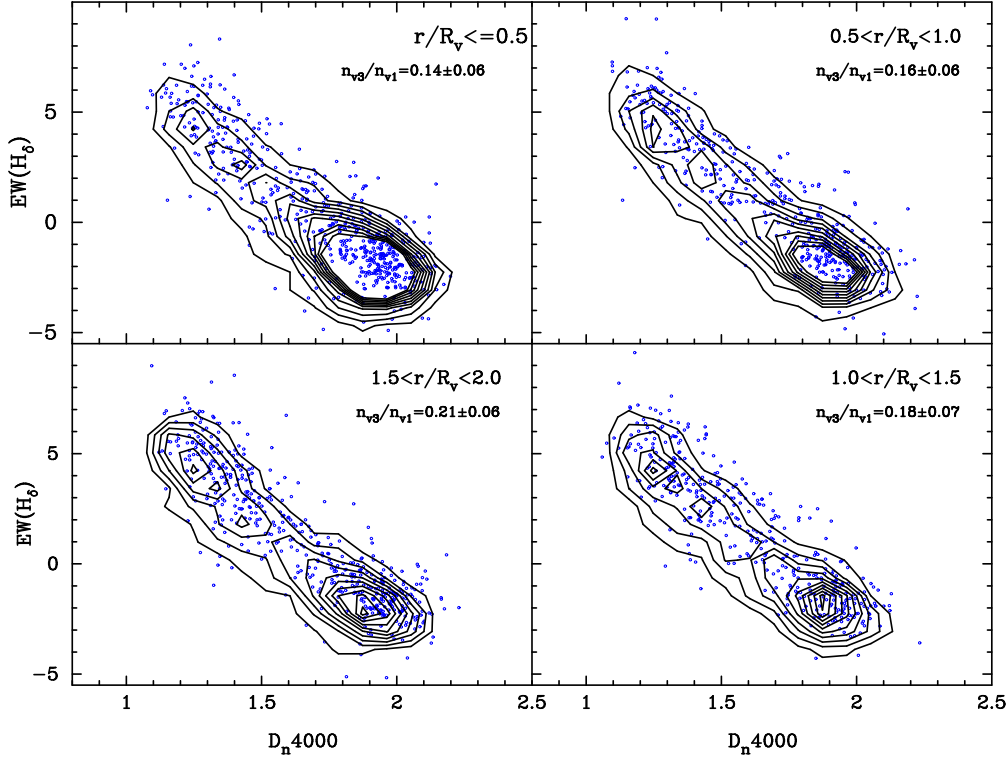


Figure 7. The distribution of galaxies having the highest ($|v_{\text{LOS}}|/\sigma_v = 2 - 3$; blue points) and the lowest ($|v_{\text{LOS}}| < \sigma_v$; black contours) absolute LOS velocity relative to the cluster, in bins of increasing (scaled) radius (*clockwise from top left*). The innermost contour represents a density of 100, decreasing by 10 at every subsequent level. The fractions in the top right corner of each panel show the ratio of the numbers in the two classes of galaxies shown, and the scatter in it. Barring the innermost radial bin, the distribution of high velocity galaxies remains the same, although the distribution of the virialised galaxies tends to become bimodal with increasing (scaled) radius.

Figs. 5 and 6 show the distributions of $\text{EW}(\text{H}\delta)^4$ and D_n4000 for the galaxies in 12 different cells of projected phase space (three scaled absolute LOS velocities times four scaled projected radii), and compare them with the distribution of field galaxies. The $\text{EW}(\text{H}\delta)$ distribution of the cluster galaxies is strikingly different from that of the field galaxies, the latter showing a bimodality at $\text{EW}(\text{H}\delta) \sim 2 \text{ \AA}$ (also see Table A5). In the cluster cores, the galaxies with highest velocities, which are most likely to have fallen in recently (Table 1), are the ones that also show $\text{H}\delta$ in absorption ($\text{EW}(\text{H}\delta) > 0$). This suggests that their likelihood of experiencing a burst of star formation within the last $\sim 1 - 3 \text{ Gyr}$ is relatively higher than their low velocity counterparts. The K-S test shows that the difference between the $\text{EW}(\text{H}\delta)$ distributions of the highest and the lowest absolute LOS velocity galaxies is statistically significant at all radii within $1.5 R_v$ (Table A5).

The amplitudes of the 4000 \AA break in SDSS galaxy spectra show very different distributions for the highest and lowest classes of $|v_{\text{LOS}}|$, both in the core ($< 0.5 R_v$) and on the periphery ($1 - 1.5 R_v$) of the clusters. However, the distributions of D_n4000 in

the $0.5 - 1 R_v$ bin are only very marginally dissimilar, with $\sim 10\%$ probability of the null hypothesis being satisfied (see Table A6).

We now take advantage of the fact that together $\text{H}\delta$ and D_n4000 yield a good constraint on the SFHs (Kauffmann et al. 2003) of galaxies. In Fig. 7 we show the SFHs of galaxies with different absolute LOS velocities in bins of increasing cluster-centric radius. For clarity, we only plot the two extreme absolute LOS velocity classes ($|v_{\text{LOS}}| < \sigma_v$ and $|v_{\text{LOS}}|/\sigma_v = 2 - 3$). The distribution of the low $|v_{\text{LOS}}|$ galaxies, in this plot of $\text{EW}(\text{H}\delta)$ vs D_n4000 , is dominated by the passive sequence (lower right) at low projected radii, and becomes increasingly bimodal with increasing cluster-centric radius. The same evolution occurs for the high $|v_{\text{LOS}}|$ galaxies, but is less bimodal at large projected radius. On the other hand, the high absolute LOS velocity galaxies span the entire available parameter space equally at all distances. According to the stellar population study of Kauffmann et al. (see their fig. 3), this is an indication that the SFH is more continuous in the low $|v_{\text{LOS}}|$ galaxies and star formation occurs more in bursts in the high velocity galaxies. We discuss these trends in the context of the relative fraction of the infalling and backsplash galaxies, and the fraction of star-forming galaxies as a function of cluster-centric distance in §5.

We now refer to galaxies with $\text{EW}(\text{H}\delta) > 2$ and $D_n4000 < 1.5$ as *Galaxies with Ongoing or Recent Efficient Star formation* (GORES), following the assumption that a galaxy that experienced efficient star formation $\lesssim 1 - 3 \text{ Gyr}$ ago is likely to show these features prominently in its spectrum. Our choice of $\text{EW}(\text{H}\delta)$ and D_n4000 thresholds are based on the bimodality seen in the field distributions (Figs. 5 and 6).

Fig. 8 shows how the fraction of GORES, f_{GORES} , varies

⁴ Note that the negative values of $\text{EW}(\text{H}\delta)$ do not imply $\text{H}\delta$ line emission in the passive galaxies, because the $\text{EW}(\text{H}\delta)$ values are measured from the pseudo-continuum bands, and so do not always represent the ‘true’ flux in the $\text{H}\delta$ line. The pseudo-continuum bands are required because in the spectra of passive galaxies, the position of several metal lines may coincide with the $\text{H}\delta$ line, making it virtually impossible to measure the ‘true’ flux (G. Kauffmann, priv. comm.; see also Worthey & Ottaviani 1997 and Kauffmann et al. 2003).

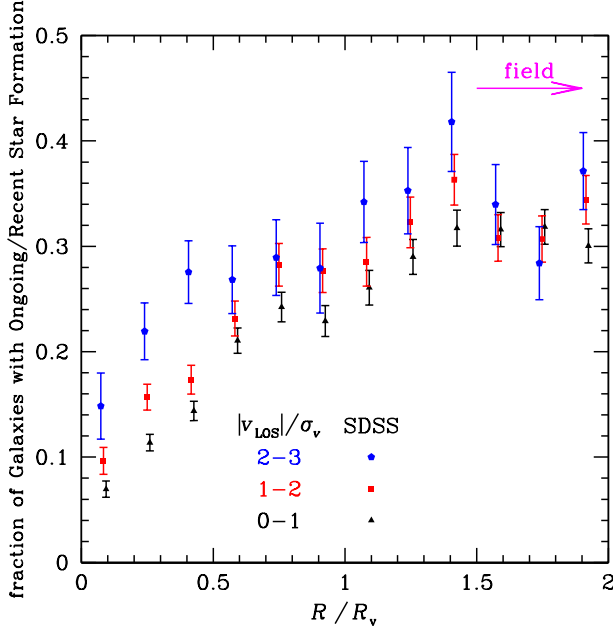


Figure 8. The fraction of Galaxies with Ongoing or Recent Efficient Star Formation (GORES, $\text{EW}(\text{H}\delta) > 2 \text{ \AA}$ and $\text{D}_{n4000} < 1.5$) versus projected radius in bins of absolute LOS velocity: $0 - 1 \sigma_v$ (black triangles), $1 - 2 \sigma_v$ (red squares), and $> 2 \sigma_v$ (blue pentagons), slightly shifted along the x -axis for clarity. The magenta arrow indicates the GORES fraction in the field ($R > 3 R_v$).

with projected radius and absolute LOS velocity. The generally increasing radial trend of f_{GORES} is clearly modulated by $|v_{\text{LOS}}|$: at all projected radii, the value of f_{GORES} is higher (lower) for high (low) $|v_{\text{LOS}}|$.

4 MODELLING THE VELOCITY MODULATION

In this section, we present simple models to quantify the observed fraction of GORES by combining theoretical predictions with the suite of galaxy properties analysed in §3.

We build two simple models of the frequency of GORES, one in which their frequency only depends on the *class* of galaxies, i.e. whether they are part of the virialised, infall or backplash population, and second, where the frequency of GORES depends upon class *and* the distance from the centre of the cluster. We define the three classes of galaxies in radial phase space (i.e. $[r, v_r]$, where r is the 3D radius and v_r the radial velocity) using the $z = 0$ output of a cosmological simulation. We also use this simulation to project these quantities onto the observable *projected phase space*, $[R, |v_{\text{LOS}}|]$, where R is the projected radius.

4.1 Cosmological simulation

We use the high-resolution cosmological hydrodynamical simulation run by Borgani et al. (2004). To summarise, the simulation assumes a cosmological model with $\Omega_0 = 0.3$, $\Omega_\Lambda = 0.7$, $\Omega_b = 0.039$, $h = 0.7$, and $\sigma_8 = 0.8$. The box size is $L = 192 h^{-1} \text{ Mpc}$. The simulation uses 480^3 DM particles and (initially) as many gas particles, for a DM particle mass of $4.62 \times 10^9 h^{-1} \text{ M}_\odot$. The softening length was set to $22.5 h^{-1}$ comoving kpc until redshift $z = 2$ and fixed

for subsequent epochs (i.e., at $7.5 h^{-1} \text{ kpc}$). DM halos were identified by Borgani et al. at redshift $z = 0$ by applying a standard FoF analysis to the DM particle set, with linking length 0.15 times the mean inter-particle distance. After the FoF identification, the centre of the halo was set to the position of its most bound particle. A spherical overdensity criterion was then applied to determine the virial radius, R_{200} of each halo. In this manner, 117 halos were identified within the simulated volume, of which 105 have virial mass M_{200} greater than $10^{14} h^{-1} \text{ M}_\odot$. To save computing time, the subsequent analysis was performed on a random subsample of roughly 2 million particles selected from the whole sample of 480^3 particles. We deliberately chose to analyse DM particles rather than galaxies in the simulations, as we do not trust the galaxy distribution, with a homogeneous core found in these and other hydrodynamic cosmological simulations, as they conflict with the observations (Saro et al. 2006). Moreover, the particle data provide much better statistics.

A sample of 93 non-bimodal mock clusters were extracted from these simulations by Mamon, Biviano, & Murante (2010), who placed their observer at $90 h^{-1} \text{ Mpc}$ of each mock cluster and added the peculiar motions to the distance with the Hubble constant value ($H_0 = 100 \text{ km s}^{-1} \text{ Mpc}^{-1}$) corresponding to the units of positions ($h^{-1} \text{ kpc}$). This yields fairly regular clusters that should resemble those of Yang et al. (2007) (in the latter case, their high threshold causes multimodal clusters to be fragmented into several). We repeated the same extraction, this time with by placing the observer at an infinite distance of each cluster (cylindrical projection).

4.2 Classification schemes

Ideally, one should define the virial, infall and backplash classes by following the orbits of the particles (Gill et al. 2005), but this task is beyond the scope of the present article. Instead, we define the classes using the present-day radial phase space distribution of particles. Particles that are outside the virial radius, and travelling at velocities lower than the critical velocity, are falling into the cluster for the first time, while particles outside the virial radius with higher velocities must have crossed the cluster at least once.

Sanchis, Łokas, & Mamon (2004) have analysed the distribution of DM particles in the radial phase space (r, v_r) at $z = 0$, for a cluster-mass halo in a dissipationless cosmological n -body simulation (256^3 particles in a box of $150 h^{-1} \text{ Mpc}$ width). Their fig. 1 (see also Mamon et al. 2004) suggests that the separation of particles belonging to the infall, backplash and virialised populations can be written with a critical radial velocity delimiting the infall regime from the other two classes:

$$\frac{v_{r,\text{crit}}}{V_v} = -1.8 + 1.06 \left(\frac{r}{R_v} \right). \quad (2)$$

Fig. 9 shows the distribution of DM particles in the stack of 93 clusters in radial phase space (r, v_r). Overplotted are the cuts of Sanchis et al. (2004) designed to separate the virialised, infall, and backplash classes of particles (Eq. 2). The particles within the virial radius with large absolute radial velocities have uncertain classes.

We devise several *Schemes* to identify the three classes of particles (we refer to fig. 6 in Bertschinger 1985 for a schematic view of the trajectories of particles in radial phase space). Table 1 summarises these schemes. The rapidly infalling particles with $r < r_v$ might represent the low-end tail of the radial velocity distribution

Table 1. Schemes of particle classes from positions in radial phase space

Scheme	Region r/R_v	A < 1 $v_r > -v_{r,crit}$	B < 1 $v_{r,crit}^{(2)} \leftrightarrow v_{r,crit}$	C < 1 $< v_{r,crit}^{(2)}$	D > 1 $v_{r,crit}^{(2)} \leftrightarrow v_{r,crit}$
0		virial	virial	virial	infall
1		virial	infall	infall	infall
2		backsplash	infall	infall	infall
3		infall	infall	infall	infall
4		backsplash	backsplash	backsplash	infall
5		backsplash	backsplash	infall	backsplash

1

Note: The letters A to D correspond to the regions in Fig. 9. The symbol \leftrightarrow means ‘in between’.

of the virial class, which we denote by Scheme 0, or might indeed be part of the infall class (Schemes 1 to 3), or may even be mainly populated by particles on their second infall, i.e. backsplash class (Scheme 4). The rapidly expanding particles with $r < r_v$ might again represent the high-end tail of the radial velocity distribution of the virial class (Schemes 0 and 1), or the backsplash class (Schemes 2 and 4), or the infall class (if the star forming properties of galaxies in this region of radial phase space reflect those of the rapidly infalling class within the virial radius, Scheme 3). Scheme 0 corresponds to maximum virialisation while Scheme 3 corresponds to maximum infall.

Although Fig. 9 is based upon a very different simulation (hydrodynamical instead of dissipationless and with three times better mass resolution) and on a stacked halo instead of a single one, it shows that the critical radial velocity of Eq. 2 is fully adequate to distinguish between infalling and backsplash particles in the stacked mock cluster obtained from the cosmological hydrodynamical simulation analysed here.

One may argue that the red solid line separating the infall and backsplash classes is too high and that we may be missing an important fraction of backsplash particles at high r and low v_r . We thus created a *maximum backsplash* Scheme 5, where we consider the critical velocity

$$\frac{v_{r,crit}^{(2)}}{V_v} = -2.2 + 0.83 \left(\frac{r}{R_v} \right). \quad (3)$$

This is shown as the magenta dashed line in Fig. 9: particles with $v_r < v_{r,crit}^{(2)}$ are infalling, other particles are backsplash or virial according to Scheme 4 applied with $v_{r,crit}$.

The cosmological simulation provides us with a unique way of measuring the frequency of the three classes of particles (galaxies) in projected phase space. We translate velocities from $V_v = V_{100}$ to the observable cluster velocity dispersion, σ_v , noting that the stacked cluster has a velocity dispersion (limited to the aperture $r < R_v$) of $0.65 V_v$, as measured in the hydrodynamical simulation by Mamon et al. (2010), and within 5% of what is expected for isotropic NFW models of clusters (Appendix A of Mauduit & Mamon 2007).

Fig. 10 shows the fractions of the three classes in projected phase space. The virialised particles are necessarily at radii $r < R_v$, the infalling particles prefer large projected distances and high velocities, while the backsplash particles are mostly found just around the virial radius and have *low absolute LOS velocities*. This preference of backsplash galaxies for low $|v_{LOS}|$ is an immediate conse-

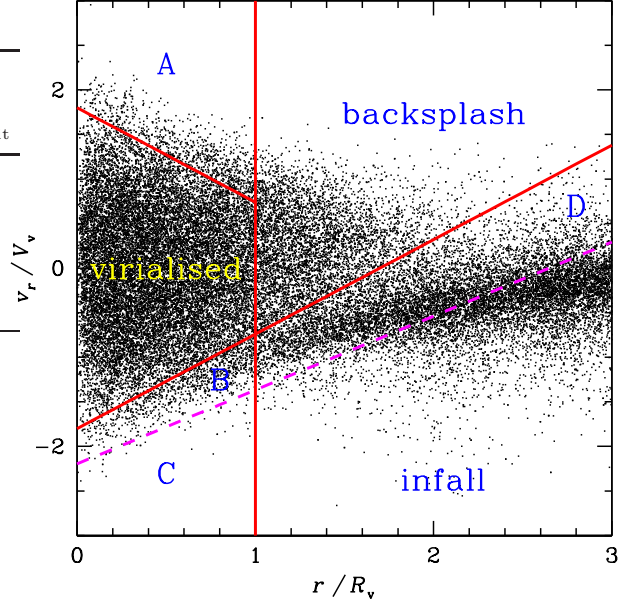


Figure 9. Radial phase space distribution of dark matter particles of the stack of 93 regular mock clusters from the cosmological hydrodynamical simulation of Borgani et al. (2004). The units of radius and radial velocity are the virial radius r_{100} and the circular velocity at that radius, respectively. The critical velocity separating infall from backsplash population (long diagonal red line) is given in Eq. 2. The short diagonal line represents the negative critical velocity threshold (see §4). For clarity, only 1 out of 550 particles of the original simulation is plotted. Region A is virialised in Schemes 0 and 1, infall in Scheme 3, and otherwise backsplash. Region B is virialised in Scheme 0, infall in Schemes 1 to 3, otherwise backsplash. Region C is virialised in Scheme 0, backsplash in Scheme 4, otherwise infall. Region D is backsplash in Scheme 5, otherwise infall (see Table 1).

quence of their lower radial velocities (§1) and has also been noted by Gill et al. (2005).

In the top panel of Fig. 11, we show the contours for the fraction of particles that are backsplash, while the bottom panel provides the fraction of backsplash particles versus projected radius in wide bins of absolute LOS velocity. The two plots of Fig. 11 indicate that the fraction of backsplash particles reaches a maximum of 54% just outside the virial radius at very low $|v_{LOS}|$ for Scheme 3 (75% for Scheme 5). At high $|v_{LOS}|$, the fraction of backsplash particles is symmetric relative to the virial radius. However, at low $|v_{LOS}|$, the fraction is skewed towards higher values beyond the virial radius (see, e.g. curve representing all particles with $|v_{LOS}| < 3\sigma_v$ in the bottom panel of Fig. 11). Indeed, at projected radii smaller than the virial radius, the backsplash particles must be in the foreground or background of the virial sphere, and geometric effects typically cause their 3D velocities to be aligned with the line of sight, making it difficult to obtain small absolute LOS velocities. These trends are confirmed in Table 2, which lists the fractions of the three classes of particles in cells of projected phase space.

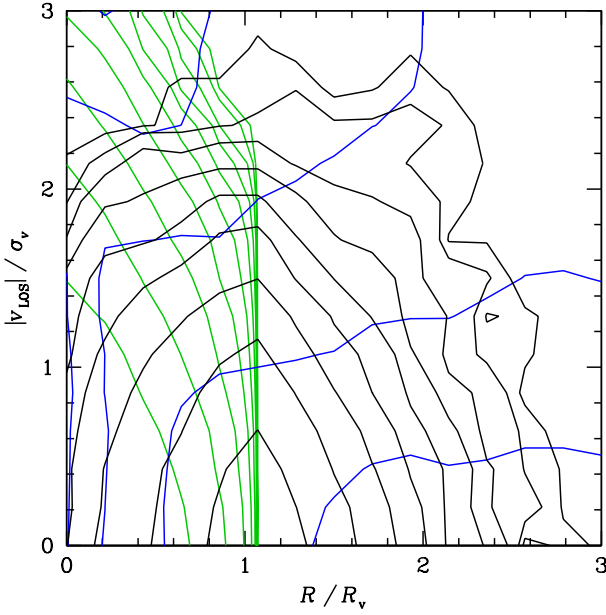
4.3 Models

4.3.1 Global deprojection

We first directly deproject the observed fractions of GORES, regardless of the LOS velocity. Expressing the global (sum-

Table 2. The fraction of virialised (v) infall (i) and backslash (b) particles of the stacked mock cluster in cells of projected phase space with Scheme 3

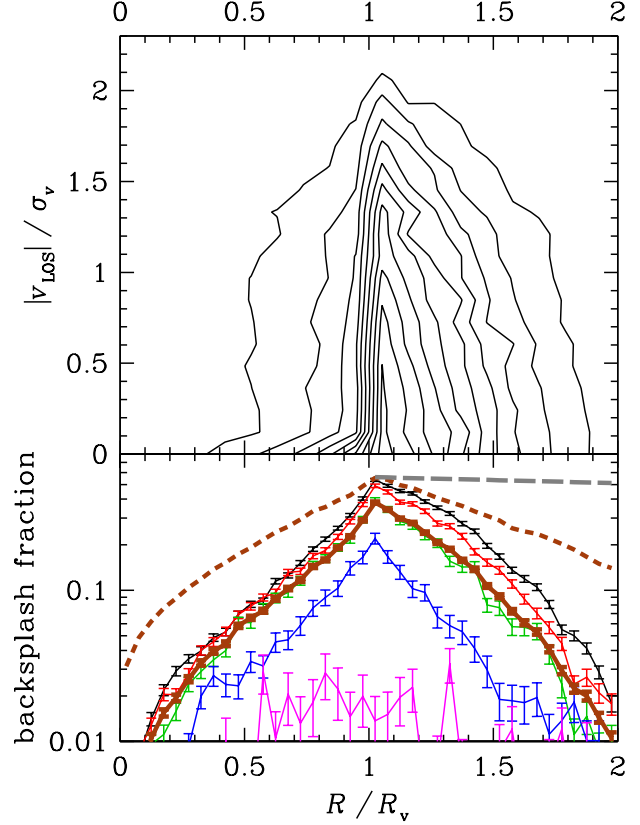
r/R_v $ v_{\text{LOS}} /\sigma_v$	0–0.5			0.5–1			1–1.5			1.5–2		
	v	i	b	v	i	b	v	i	b	v	i	b
0–1	0.89	0.08	0.03	0.49	0.33	0.18	0.00	0.65	0.35	0.00	0.93	0.07
1–2	0.83	0.16	0.02	0.40	0.48	0.11	0.00	0.81	0.19	0.00	0.97	0.03
2–3	0.69	0.31	0.00	0.16	0.83	0.01	0.00	0.99	0.01	0.00	1.00	0.00

**Figure 10.** Density in projected phase space of virial (green), infall (blue) and backslash (black contours) particles of the stacked mock cluster with our preferred model (Scheme 3, see Fig. 9). The contours are logarithmically spaced by a factor of 2.3, and the same set of contours is used for all three classes: the highest contours are on the lower left (virial), lower right (infall) and bottom (backslash), where the latter two classes only reach the 2nd highest contour of the virial class.

ming over the velocity bins) observed fraction of GORES as $g_{\text{GORES}}(R) = N_{\text{GORES}}(R)/N_{\text{tot}}(R)$, we can deduce the surface densities, $\Sigma(R) = N(R)/(2\pi R dR)$ of GORES and of all galaxies. Since the projected number profiles $N_{\text{GORES}}(R)$ and $N_{\text{tot}}(R)$ are fairly noisy, we fit a polynomial to $\log \Sigma$ vs. $\log R$ and extrapolate the data beyond the last point by a power-law, whose slope is fit on the last three points. Fig. 12 shows the surface density profiles and their polynomial fits. While the fits diverge dramatically at low R , they match remarkably well at high R (better than analogous fits of $\log \Sigma$ vs. R , not shown in Fig. 12 for clarity). One can now perform Abel inversion to deduce the space densities

$$\nu(r) = -\frac{1}{\pi} \int_r^\infty (d\Sigma/dR) / \sqrt{R^2 - r^2} dR \quad (4)$$

of GORES and all galaxies, and finally obtain the deprojected fraction of GORES by dividing the two space densities. Fig. 13 shows the resultant deprojected fraction of GORES, obtained with the orders 3 to 5 polynomial fits of $\log \Sigma$ vs. $\log R$ (Fig. 12). Fig. 13 also shows a χ^2 fit of Eq. 5 to the deprojected fraction of GORES obtained from the order 4 polynomial fit of $\log \Sigma$ vs. $\log R$, using

**Figure 11.** Upper panel: contours in projected phase space of the fraction of particles of the stacked mock cluster that contribute to the backslash class (Scheme 3; see Fig. 9). Contours are linearly spaced from 0.05 to 0.5 going downwards. Lower panel: fraction of backslash particles in bins of absolute LOS velocity: 0–0.5 (top, black), 0.5–1.0 (red), 1.0–1.5 (green), 1.5–2.0 (blue), and $> 2.0 \sigma_v$ (bottom, magenta), and summed over all LOS velocities $< 3 \sigma$ (thick brown). The dashed thick brown curve shows the maximum backslash fraction (for $|v_{\text{LOS}}| < 3 \sigma_v$) from Scheme 5 while the long-dashed thick grey line is the relation deduced from observations by Pimbblet (2011) (see §5.3).

$$f_{\text{GORES}}(r) = f_0 \frac{r}{r + a}. \quad (5)$$

We see that the simple, saturated linear model provided in Eq. 5, with asymptotic GORES fraction $f_0 = 0.52$ and quenching radius for efficient star formation (hereafter quenching radius) $a = 1.26 R_v$, is a decent representation of the deprojected profile for f_{GORES} . While this deprojection leads to an asymptotic value of $f_{\text{GORES}} = 0.52$, Eq. 5 yields $f_{\text{GORES}} = 0.44$ at our typical minimum projected radius for field galaxies ($6.7 R_v$), very close to their observed fraction of 0.45.

Note that although the constraints from potential SDSS fibre

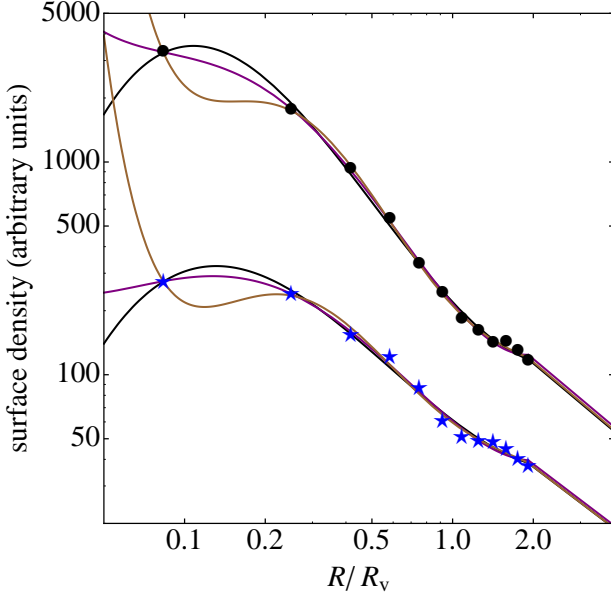


Figure 12. Surface density of all galaxies (*top*) and of GORES (*bottom*). The symbols are the data (filled black circles for all galaxies and blue stars for GORES). The black, purple, and brown curves represent the polynomial fits of $\log \Sigma$ vs $\log R$ for orders 3, 4, and 5, respectively. The data were extrapolated beyond $2 R_v$ with power-law fits to the outermost three data points.

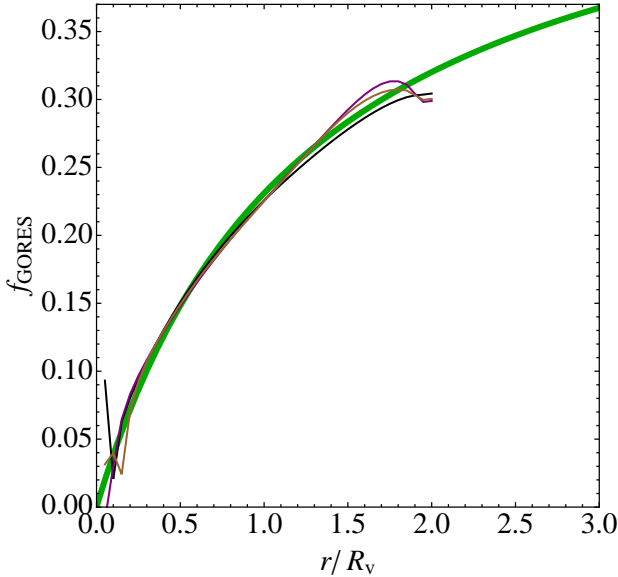


Figure 13. Deprojected fractions of GORES (using Eq. 4). Thin curves show the results obtained by polynomial fits of the log surface density vs $\log R$ (orders 3, 4, and 5 in black, purple and brown, respectively). The thick green curve represents Eq. 5 with $f_0 = 0.52$ and $a = 1.26 R_v$, obtained by a χ^2 fit to the order 4 polynomial fit of $\log \Sigma$ vs $\log R$ (purple curve), with r linearly spaced between 0.05 and $2 R_v$.

Table 3. Best-fit parameters for the 3 galaxy classes with the 6 schemes for the model of constant GORES fraction per class

Scheme	$r < R_v$ AND		f_v	f_i	f_b	χ^2_ν
	$v_r < v_{r,\text{crit}}$	$v_r > -v_{r,\text{crit}}$				
0	virial	virial	0.11	0.33	0.26	4.6
1	infall	virial	0.10	0.34	0.24	3.5
2	infall	backsplash	0.10	0.33	0.28	2.9
3	infall	infall	0.10	0.34	0.23	2.7
4	backsplash	backsplash	0.09	0.32	0.32	3.0
5	backsplash*	backsplash	0.10	0.33	0.30	2.9

Notes: χ^2_ν is the χ^2 per degree of freedom. The errors are typically 0.01 on f_v and f_i and 0.04 on f_b . In Scheme 5, the extreme negative velocities for $r < R_v$ correspond to infall galaxies.

collisions leads to underestimated surface density profiles at low projected radii, this bias in surface density should affect both the total and GORES surface densities in a similar (multiplicative) way (Eq. 4). Hence the effect of fibre collisions on the ratio of GORES to total space densities should be minor.

We now refine the models accounting for the LOS velocity modulation of $f_{\text{GORES}}(R)$, using the dynamical classes of the galaxies (virial, infall, and backsplash).

4.3.2 Model 1: Constant recent starburst fraction per class

Suppose that for each of the three classes of galaxies (virial, infall and backsplash), the fraction of galaxies which experienced a recent ($\lesssim 1 - 3$ Gyr) starburst (GORES) is independent of the 3D radius and radial velocity. Let these three fractions be f_v , f_i and f_b respectively (we drop the subscript ‘GORES’ from f for clarity).

The fraction of GORES in a cell (R, v_z) of projected phase space can then be written as

$$g_{\text{GORES}}(R_i, v_j) = \sum_{\alpha} f_{\alpha} p(\alpha | R_i, v_j), \quad (6)$$

where, $p(\alpha | R_i, v_j)$ is the fraction of particles of class α within the cell (R_i, v_j) of projected phase space (as in Table 1, but with finer radial bins).

One can then perform a χ^2 fit between the observed and predicted fractions of GORES $g_{\text{GORES}}(R_i, v_j)$ over all cells (R_i, v_j) , using the conditional probabilities for each class, $p(\alpha | R_i, v_j)$, derived from the cosmological simulation. We assume binomial error bars on the observed values of $g_{\text{GORES}}(R_i, v_j)$ and that the $p(\alpha | R_i, v_j)$ derived from the cosmological simulation are perfectly known. Furthermore, we use the six Schemes for the three populations, changing the class within the cluster virial sphere for the extreme velocities $|v_r| > |v_{r,\text{crit}}(r)|$ as explained in the caption of Fig. 9. Table 3 shows the best fits for each of these six population schemes.

The best-fit predictions for the scheme with the lowest reduced χ^2 (hereafter χ^2_ν), Scheme 3 (where both the very positive and very negative radial velocity objects within the virial sphere are considered to be part of the infall population), provide a reasonable match to the observed fractions of GORES in bins of projected phase space. But $\chi^2_\nu = 2.7$ for this best-fit model, suggests that the model itself can be improved.

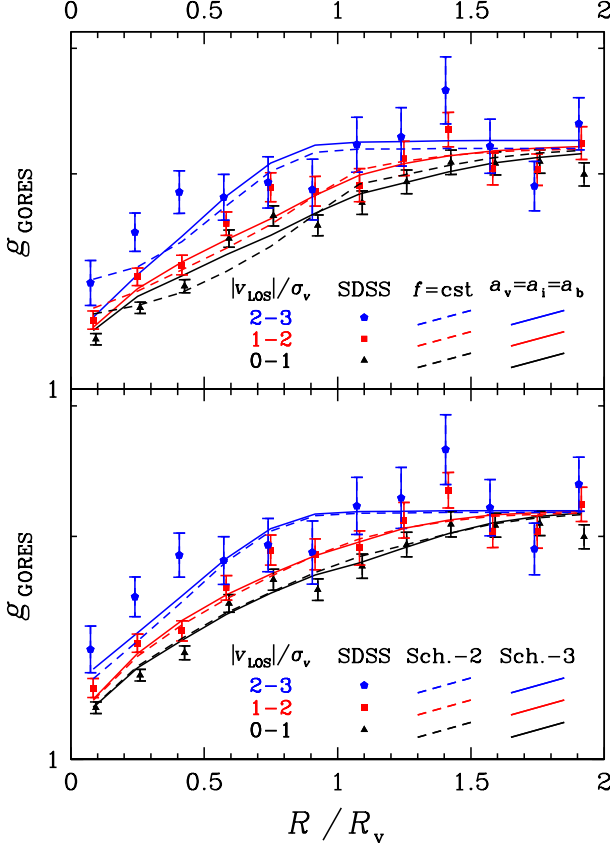


Figure 14. Same as Fig. 8, with best fit models overplotted: *Top:* the *dashed* and *solid* curves show the best-fit Scheme 3 models (Tables 3 and 4) assuming no radial dependence (using Eq. 6) and the radially varying one of Eq. 7, forcing $a_v = a_i = a_b$, using Eq. 8, respectively. *Bottom:* Best-fit radially varying model (Eq. 7) with free values of a_v , a_i , and a_b , for Schemes 2 (*dashed*) and 3 (*solid*). The schemes are defined in Tables 3 and 4.

4.3.3 Model 2: Recent starburst fractions increasing with physical radius

In our second model, we suppose that the fraction of GORES is no longer constant per class, but varies with physical radius r as in Eq. 5, varying the normalisation and scale for each class:

$$f_\alpha(r) = f_\alpha \frac{r/R_v}{r/R_v + a_\alpha}, \quad (7)$$

i.e. rising roughly linearly with radius for $r < a_\alpha$, and saturating to an asymptotic value f_α at large radii. The predicted fractions of GORES is then

$$g_{\text{GORES}}(R_i, v_j) = \sum_\alpha p(\alpha|R_i, v_j) \sum_k f_\alpha(r_k) q(r_k|R_i, v_j, \alpha), \quad (8)$$

where $q(k|R_i, v_j, \alpha)$ is the fraction of the particles of class α in the cell of projected phase space (R_i, v_j) that are in the k th bin of physical radius. The physical radial bins are expressed as $r_k = R_i \cosh u_k$, where u_k is linearly spaced from 0 to $\cosh^{-1} r_{\text{max}}/R_i$, using $r_{\text{max}} = 50 R_v$.

Table 4 shows the new set of fits. The first set of lines shows the fits when we force the same quenching radius for the three classes: $a_v = a_i = a_b$. Again, Scheme 3 provides the lowest χ^2_ν , which is now 1.6 (in comparison with 2.7 for the $f = \text{constant}$ model). So with the inclusion of just one extra parameter, the

radially-varying model fits the data much better. This is confirmed with both the F -test and the AICc (Akaike 1974; Hurvich & Tsai 1989) criterion (Table 4). Note that cosmic variance on the finite number of clusters has been incorporated in the errors. The value of quenching radius a is low in Scheme 3, which indicates that it is not that far from the model with constant fraction of GORES per class. The top panel of Fig. 14 shows the observed fractions of GORES together with the best fits with Scheme 3 for both the constant fraction per class and radially-varying models with $a_v = a_i = a_b$. Both models capture the initial rise of the GORES fraction with projected radius and subsequent saturation, as well as the velocity modulation, even though the fit is not excellent.

In the next set of fits, shown in the bottom six rows of Table 4, we lift the assumption of $a_v = a_i = a_b$. The best-fit reduced χ^2 values are now ≤ 1.6 for Schemes 1–5, with an often significant improvement of the fit (despite the two extra parameters) over the radially-varying model with the same scale parameters (see the F test statistic in Table 4). The F -test indicates that the improvement is significant with the inclusion of two extra parameters (three scales instead of a unique one). Using the Akaike criterion, which reduces here to $\Delta\text{AICc} = \Delta\text{AIC} = \Delta\chi^2$, with associated probability $P = \exp(-\Delta\text{AIC}/2)$, we conclude that Scheme 3, which still leads to the lowest $\chi^2_\nu = 1.2$, is a significantly better fit than Scheme 0 (99.7% confidence) and marginally significantly better fit than Schemes 4 (93% confidence) and 5 (94% confidence). Although a decent fit to the data, this best-fit model still predicts too low values of f_{GORES} for high absolute LOS velocity galaxies within half virial radius of the clusters. Interestingly, the best-fit model (Scheme 3) predicts a constant GORES fraction for the infall class galaxies ($a_i = 0$), while the next best-fitting model (Scheme 2) predicts that both infall and backslash populations have a constant GORES fraction ($a_i = a_b = 0$).

5 DISCUSSION

This paper is a unique analytical effort to explore the variations in the spectral and physical properties of different dynamical classes of galaxies residing in similar environments projected on the observed sky (projected radius and absolute LOS velocity), and to interpret these differences. We draw a sample of $\sim 20,000$ galaxies ($M_r \leq -20.5$) found within $2R_v$ and $|\Delta v_{\text{LOS}}| < 3\sigma_v$ of 268 galaxy clusters, and a similar sample of field galaxies for this purpose. All the galaxies are taken from the SDSS DR4 spectroscopic galaxy catalogue.

5.1 Velocity segregation of stellar mass

Three physical mechanisms might explain the excess of high mass galaxies in the cluster cores amongst the low velocity galaxies (Fig. 2): cluster tides, two-body relaxation, and dynamical friction. We examine in turn each one of these.

Tidal effects from the cluster gravitational field (predicted by Merritt 1983; Mamon 1992; Gnedin, Hernquist, & Ostriker 1999, clearly seen in cosmological simulations by Ghigna et al. 1998, and measured through gravitational lensing by Natarajan et al. 2009) will be most effective on slowly moving galaxies, because these have more time to feel the cluster tides. Even though stars are less affected by tides than the more extended dark matter haloes, simulations of a live dwarf spiral galaxy orbiting a spiral galaxy ~ 100 times more massive, with fixed gravitational potential (Klimontowski et al. 2009) or live N -body system

Table 4. Best-fit parameters for the three galaxy classes with the four schemes for models of radially-varying GORES fraction

Scheme	$r < R_v$ AND		f_v	f_i	f_b	a_v	a_i	a_b	χ^2_ν	F	P_F	ΔAICc	P_{AICc}		
	$v_r < v_{r,\text{crit}}$	$v_r > -v_{r,\text{crit}}$												AIC-AIC(3)	P
0	virial	virial	0.32	0.38	0.35	0.58	0.58	0.58	2.0	46	0	87	0		
1	infall	virial	0.24	0.37	0.29	0.36	0.36	0.36	1.8	31	0	55	0		
2	infall	backsplash	0.21	0.36	0.30	0.28	0.28	0.28	1.7	24	0	39	0		
3	infall	infall	0.19	0.36	0.26	0.22	0.22	0.22	1.6	24	0	36	0		
4	backsplash	backsplash	0.23	0.35	0.35	0.35	0.35	0.35	1.8	24	0	40	0		
5	backsplash*	backsplash	0.22	0.36	0.34	0.31	0.31	0.31	1.8	22	0	37	0		
0	virial	virial	0.41	0.35	1.00	0.88	0.27	4.79	2.0	0.6	0.56	-3	—	11.8	0.003
1	infall	virial	0.34	0.34	0.36	0.72	0.00	1.23	1.6	3.6	0.04	5.7	0.06	7.6	0.02
2	infall	backsplash	0.30	0.33	0.21	0.62	0.00	0.00	1.5	3.8	0.03	5.5	0.06	4.4	0.11
3	infall	infall	0.29	0.34	0.39	0.62	0.00	1.40	1.2	5.7	0.01	8.3	0.02	—	—
4	backsplash	backsplash	0.26	0.37	0.28	0.50	0.55	0.00	1.6	3.1	0.06	4.1	0.13	5.4	0.07
5	backsplash*	backsplash	0.27	0.35	0.27	0.53	0.19	0.00	1.6	2.8	0.08	3.4	0.19	5.7	0.06

Notes: The upper portion is for fits in which $a_v = a_i = a_b$ is enforced, while the lower portion is for fits with fully free scale radii. The errors are typically 0.01 on f_v and f_i and 0.04 on f_b . In Scheme 5, the extreme negative velocities for $r < R_v$ are infall. The best fitting scheme 3 is highlighted in bold. F and P_F represent the F test statistic that the fit with the scheme is significantly better than that of the previous model ($f(r)$ with $a_v = a_i = a_b$ vs. $f = \text{cst}$ for the upper panel and general $f(r)$ vs. $f(r)$ with $a_v = a_i = a_b$ for the lower panel) and the associated probabilities of a larger value of F appearing by chance.

ΔAICc and P_{AICc} represent the same quantities with the Akaike criterion ($\text{AIC} = \chi^2 + 2k$, for k parameters, Akaike 1974) modified for finite size samples ($\text{AICc} = \chi^2 + 2k n / (n - k - 1)$, for k parameters and n data points, Hurvich & Tsai 1989). The final two columns for the lower panel provide the Akaike statistic testing whether the fit for Scheme $\neq 3$ is as good as Scheme 3 and its associated probability that a larger value of AICc occurs by chance.

(Łokas et al. 2010) indicate that, at each pericentric passage, over 35% (Klimentowski et al.) to 67% (Łokas et al.) of the stars of a spiral galaxy are tidally stripped. Tides will thus transform massive galaxies into low mass ones, and low mass galaxies into even lower mass ones. So tides cause a decrease in the fraction of high mass galaxies, which disagrees with the trend seen in Fig. 2.

If two-body relaxation can lead to energy equipartition in the cluster cores, then the high mass galaxies will move slower (in 3D). So the fraction of high mass galaxies among the low 3D velocity ones should increase with decreasing cluster-centric radius. Hence, the fraction of high mass galaxies among the low absolute LOS velocity should also increase with decreasing radius. However, the same argument would lead us to predict that the fraction of high mass galaxies among the high velocity ones should decrease with decreasing radius, and instead Fig. 2 shows no such trend. Therefore, the trend in Fig. 2 cannot be due to two-body relaxation, unless some other process is increasing the fraction of high mass galaxies among the high velocity ones within the cluster core.

The time required by dynamical friction to make the orbits of galaxies decay towards the cluster centre scales as v^3/m , where v is the 3D velocity of the galaxy of mass m . Therefore the most massive and slowly-moving galaxies should have their orbits decay the most, and be brought to even lower (projected) radius. So dynamical friction should boost the fraction of high-mass slow-moving galaxies in the cluster core. Moreover, the effects of dynamical friction should be weak for the rapidly moving galaxies. This explains the lack of trend in the fraction of high mass galaxies with projected radius for the galaxies with large absolute LOS velocities.

For dynamical friction (and tides), the high-velocity galaxies act little, if one assumes a population in virial equilibrium. Now, the infalling galaxies also tend to have high absolute radial velocities (Fig. 9), hence high absolute LOS velocities (e.g., Table 2), in fact even higher than the virialised population. So the same argument applies to the infalling galaxies: their velocities are too high to be seriously affected by dynamical friction or tides.

We note that the two-body relaxation timescale is independent

of galaxy mass m , while the dynamical friction timescale varies as $1/m$. It is easy to show that the ratio of two-body relaxation time to dynamical friction time scales as $\langle m \rangle / m$. Thus, the lack of high-velocity low mass galaxies in the inner bin of projected radii in Fig. 2, in contrast with the excess expected from two-body relaxation, is not inconsistent with the excess of high-mass galaxies at low radii observed in Figure 2 and expected from dynamical friction.

Is dynamical friction efficient enough to increase the fraction of high mass galaxies towards the centre among the slowly moving galaxies? We adopt the dynamical friction timescale that Jiang et al. (2008) carefully calibrated with a cosmological hydrodynamical simulation:

$$t_{\text{df}} \simeq 1.4 \frac{M(r)/m}{\ln[1 + M(r)/m]} \frac{r}{v_c(r)}, \quad (9)$$

where m is the galaxy mass (with its tidally stripped DM halo) and $v_c(r) = \sqrt{GM(r)/r}$ is the circular velocity at radius r . Eq. 9 incorporates the effects of elongated orbits and tidal stripping. One would like to have an idea of the physical radius of each galaxy given its projected radius and absolute LOS velocity. Fig. 15 shows the distribution of physical radii given the projected radii in our adopted bins of absolute LOS velocity. *The physical radii of the low absolute LOS velocity galaxies are close to their projected radii*, so that these low-velocity galaxies can be used to deproject radial trends. But high absolute LOS velocity galaxies appear to systematically lie very far from the virial sphere (typically $10 R_v$).

Using the relation $r \approx 1.3R$ from Fig. 15, we can estimate the dynamical friction time as a function of projected radius. Fig. 16 indicates that a galaxy (along with its dark halo) must have a total mass of at least $10^{12.45} M_\odot$, for the orbital decay time, at $R = 0.25 R_v$, to be smaller than the age of the Universe. In comparison, Yang et al. (2009, their table 4) found that in the SDSS, central group/cluster galaxies of mass $3 \times 10^{10} M_\odot$ resides in halos of mass $10^{12.2} M_\odot$. Also, according to table 4 of Yang et al., central haloes of mass $10^{12.45} M_\odot$ have corresponding galaxy masses

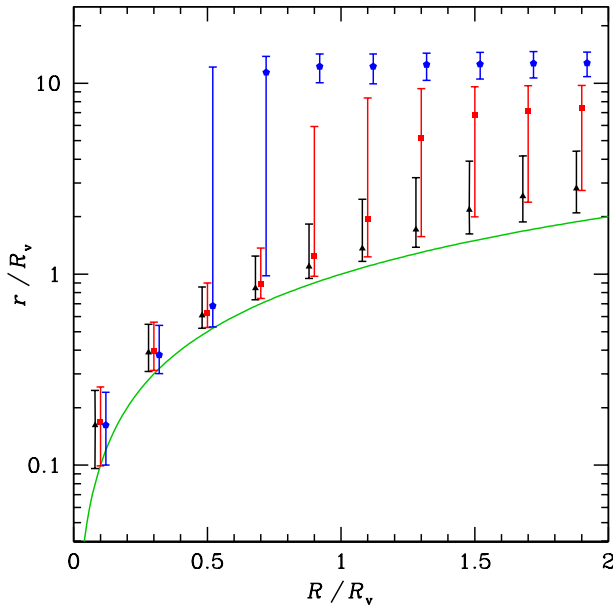


Figure 15. Physical radius versus projected radius for particles of stacked mock cluster (medians with error bars for quartiles) in bins of absolute LOS velocity: $0-1\sigma_v$ (black triangles), $1-2\sigma_v$ (red squares), and $2-3\sigma_v$ (blue pentagons). The green curve shows $r = R$.

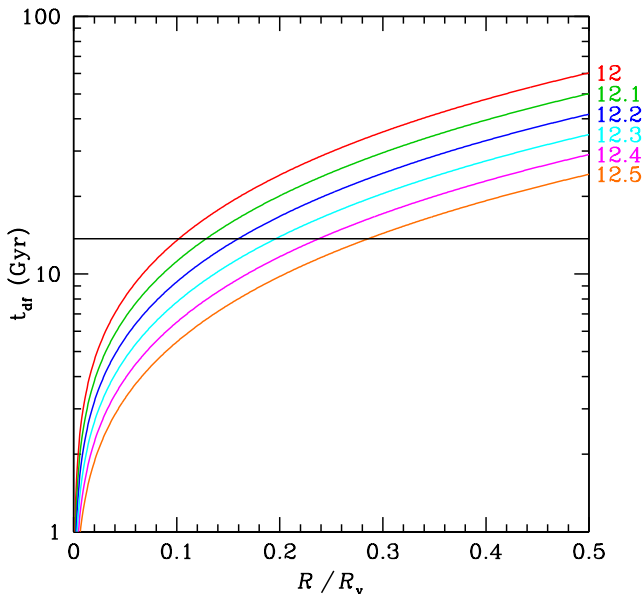


Figure 16. Timescale for orbital decay by dynamical friction versus projected radius for galaxies of log total mass (in solar masses, including the tidally stripped dark matter halo) of (from top to bottom, labelled on right) 12 (red), 12.1 (green), 12.2 (blue), 12.3 (cyan), 12.4 (magenta), and 12.5 (orange), orbiting an NFW cluster of scale radius $0.19 R_v$ and mass $M_V \equiv M_{100} = 1.9 \times 10^{14} M_\odot$ (corresponding to the median mass of $M_{180} = 10^{14.2} M_\odot$ of the SDSS clusters studied here) within the virial radius $R_v \equiv R_{100} = 1.5 \text{ Mpc}$. The timescale is estimated using Eq. 9 assuming that $r = 1.3 R$ as inferred from our cosmological simulation (see Fig. 15). The age of the Universe is shown as the horizontal line.

of $10^{10.66} M_\odot$, i.e. 45% above our galaxy mass threshold. We therefore conclude that dynamical friction might indeed be just sufficiently effective to explain the trends in Fig. 2. However, the DM halo of a galaxy extends further out than its stellar component, so halos are tidally stripped in a more efficient manner (e.g., Klimentowski et al. 2009). This means that the ratio of total to stellar mass of cluster galaxies is lower than for field galaxies. One would therefore expect the actual halo masses to be lower than inferred for the central galaxies, from table 4 of Yang et al. (2009), and thus the orbital decay times by dynamical friction to be somewhat longer.

5.2 The star-forming galaxies

The distributions of specific star formation rate, broad-band colour, and amplitude of the 4000 \AA break show statistical differences with absolute LOS velocity at almost all radii out to $R < 1.5 R_v$ (Figs. 3, 4, and 6; Tables A3, A4, and A6, respectively). However, the field component shows a bimodal distribution in $\text{EW}(\text{H}\delta)$ (Fig. 5) and D_n4000 (Fig. 6) around 2 \AA and 1.5 respectively. This is in agreement with the bimodality of these two diagnostics when plotted in terms of stellar mass, luminosity, or concentration (Kauffmann et al. 2003). We adopt these thresholds to define a galaxy as a recent starburst galaxy (GORES) if it has $\text{EW}(\text{H}\delta) > 2 \text{ \AA}$ and $\text{D}_n4000 < 1.5$.

As expected, the fraction of GORES drops within the virial radius R_v for all velocity classes (Fig. 8). But the fraction of GORES is modulated by the absolute LOS velocity: at a given projected radius, galaxies with higher $|v_{\text{LOS}}|$ have higher fractions of GORES. For the high absolute LOS velocity galaxies, the fraction of star-forming galaxies declines rapidly but only well within the core region ($\lesssim 0.5 R_v$). This once again strengthens our interpretation that the high-velocity galaxies are the youngest members of the core, having recently fallen in.

A curious feature occurs in the radial variation of both high-mass (Fig. 2) and GORES fractions (Fig. 8): the galaxies with high absolute LOS velocity show a marginally significant peak (dip) in the fraction of GORES (high mass galaxies) at $1.5 R_v$. If this feature is not a statistical fluke, it may be reflecting the discontinuity seen in SFR of cluster galaxies at the physical radius where infalling and virialised galaxies meet. However, this is expected to occur closer to the virial radius and our simple models involving the virial, infall and backslash populations do not lead to any discontinuity of f_{GORES} at $1.5 R_v$ (Fig. 14). An explanation may require a model going beyond spherical symmetry, e.g., with large-scale filaments feeding clusters (see Porter & Raychaudhury 2007; Porter et al. 2008; Mahajan et al. 2011). For the benefit of the reader, we emphasise that the enhancement seen in the SFR of galaxies seems to occur in a very narrow region only. This observation is very interesting and still being explored. It might prove useful to distinguish between the backslash and infall galaxies.

Given the M^* -SSFR anti-correlation (e.g. Mamon, Parker, & Proust 2001; Noeske et al. 2007a; Damen et al. 2009), the peak in the fraction of low mass galaxies might be directly linked to the enhancement of SFR in infalling galaxies on the outskirts of clusters before the environmental effects in clusters predominate (Porter & Raychaudhury 2007; Porter et al. 2008).

While the projected radii of the low absolute LOS velocity particles in the stacked mock cluster underestimate only slightly their physical radii (Fig. 15), our cosmological simulation indicates that the high absolute LOS velocity particles with projected radii $R > 0.8 R_v$ have very large physical radii (typically over 10 virial

radii). This implies that the observed fraction of GORES for the high absolute LOS velocity bin at $R > R_v$ should be the same as that of the field, but this is not what is observed (Fig. 8). One cannot resort to cosmic variance to explain this discrepancy, given the large number of clusters used in our analysis of the SDSS observations (268) and in the simulations (93), and we cannot find any other convincing explanation for this dichotomy.

5.3 Identifying backplash galaxies

The analysis of the $z = 0$ output of DM particles in our cosmological hydrodynamical simulation allows us to distinguish backplash particles, whose positions in radial phase space imply that they previously crossed their parent (mock) clusters from virialised particles (within the virial sphere) and the remaining infall particles (which are actually expanding away from their clusters when they are beyond the turnaround radius of $\simeq 3.5 R_v$). Our analysis in projected phase space indicates that the best place to detect backplash particles is just beyond the virial radius and at very low velocities. With Scheme 3, the backplash fraction reaches 54% (bottom panel of Fig. 11) for the lowest absolute LOS velocity bin. With the maximum backplash Scheme 5, it reaches 75% for the lowest $|v_{\text{LOS}}|$ bin.

Pimblet (2011) compared the distribution of SSFRs of galaxies with $0.3 < |v_{\text{LOS}}|/\sigma_v < 0.5$, attributed to the infall class with the full distribution. This led him to predict that the fraction of backplash galaxies decreases as $f_b = 0.61 - 0.052 R/R_v$. Such a trend (grey line in the bottom panel of Fig. 11) appears inconsistent with the backplash fractions predicted from our cosmological simulation, even with our maximum backplash Scheme 5. It is difficult to understand how one would find that as many as half of all galaxies at 2 virial radii (the maximum projected radius in the analysis of Pimblet) from clusters are backplash. Backplash galaxies typically only bounce out to 1–2 virial radii (Mamon et al. 2004).

Yet, the high fraction of backplash galaxies found by Pimblet agrees with the $54 \pm 20\%$ fraction of backplash particles that Gill et al. (2005) found in the range of projected radii $1 < R/R_v < 2$ from their cosmological simulations. In our Schemes 0–4, we find that only $17\% \pm 1\%^5$ of the particles in this range of projected radius (with $|v_{\text{LOS}}| < 3\sigma_v$) are backplash particles. However, our backplash fraction amongst DM particles is marginally consistent with the higher fraction found by Gill et al. Even in the maximum backplash Scheme 5 (partly motivated by Pimblet’s high backplash fraction, but only marginally consistent with the observed fraction of GORES), we find only $40 \pm 1\%$ of the particles in the same range of projected radius are backplash. This is apparently inconsistent with the fraction derived by Pimblet, although fully consistent with that from Gill et al.’s simulations.

Part of our disagreement with Pimblet on the fraction of backplash galaxies in the range $1 < R/R_v < 2$ may be caused by the narrow range of $|v_{\text{LOS}}|/\sigma_v$ used by him to select the infall galaxies.

5.4 The quenching of star formation in 3D: infalling vs backplash galaxies

The SDSS spectroscopy provides the means to address the role of the dynamical classes (virial, infall and backplash) in shaping the

properties of galaxies by studying the spectral features as a function of both projected radius *and* absolute LOS velocity.

Beyond the well-known radial dependence of galaxy properties in clusters, our analysis highlights the velocity modulation of these trends for the parameters SFR/M^* , $\text{EW}(\text{H}\delta)$ and the D_n4000 . All trends with projected radius are amplified with increasing absolute LOS velocity. As can be seen in Fig. 15, the effect of $|v_{\text{LOS}}|$ effectively adding to the projected radius is not trivial. Nevertheless, as qualitatively expected from the Hubble flow, in every bin of projected radius the higher absolute LOS velocities leads to higher physical radius.

In §3 we find observational evidence to support the statistical differences between the low velocity ($|v_{\text{LOS}}| \leq \sigma_v$) and the high velocity ($2 < |v_{\text{LOS}}|/\sigma_v \leq 3$) galaxies on the outskirts of clusters ($1 - 1.5 R_v$). K-S tests between the different distributions in the clusters and in the field show statistically significant differences between the low and high velocity galaxies between $1 - 1.5 R_v$ in SFR/M^* , $\text{EW}(\text{H}\delta)$ and the D_n4000 (Tables A1–A6).

Despite the noisiness of the variations with projected radius of the numbers of galaxies and of GORES, we have been able to deproject the fraction of GORES to show that it is well fit (Fig. 13) by a saturated linear model (Eq. 5). Such a model applied in turn to the three different classes of galaxy populations (virialised, infalling and backplash) with the same quenching radius ($a_v = a_i = a_b$), provides an adequate fit to the variation of GORES with projected radius in three bins of absolute LOS velocity (top four rows of Table 4 and upper panel of Fig. 14). The model reproduces the rise with projected radius and the higher fractions for higher absolute LOS velocities. Similar models with free star formation quenching radii fit the data even better (bottom four rows of Table 4 and lower panel of Fig. 14). In particular, the radius-dependent model where galaxies within the virial sphere ($r < R_v$) with radial velocity $|v_r| > |v_{r,\text{crit}}|$ are considered to be infalling, provides the best fit to the data (§4.3, Fig. 9 and Table 4).

In contrast, a simpler model, where the fraction of GORES is a constant that only depends on the class of galaxy population, does not provide an adequate fit (Table 3), even if it also reproduces these qualitative trends (Fig. 14).

The ability of Scheme 3 to better fit the SDSS data than the other three Schemes suggests that the high absolute *radial* velocity galaxies within the virial sphere, both infalling and outflowing, retain their fraction of GORES. However, our best-fit model with Scheme 2 is also an adequate fit, so the model with quenching at pericentre is also consistent with the data.

In the constant GORES fraction model with Scheme 3, the GORES fraction in the backplash class is half-way between the analogous values for the virial and infalling populations, suggesting that one passage through the cluster environment causes half the quenching of star formation. We now consider the deprojected models to assess how star formation is quenched at a unique radius where the three classes can be compared: the virial radius.

Fig. 17 shows how the best-fitting models predict the fraction of GORES as a function of the 3D radius. We first note that for the constant f_{GORES} per class model, the mean variation of f_{GORES} (top panel of Fig. 17) departs more strongly from the global trend found by the global deprojection (§4.3.1) than do the mean variations with the other models. This reinforces the view that the constant f_{GORES} per class model does not reproduce well our data.

With the radially-dependant model of the GORES fraction with equal quenching scale radii, again with Scheme 3, the fraction of GORES in the backplash population at $r = R_v$ is intermediate

⁵ The errors in our fractions of backplash particles are from 50 bootstraps on the 93 halos of the cosmological simulation.

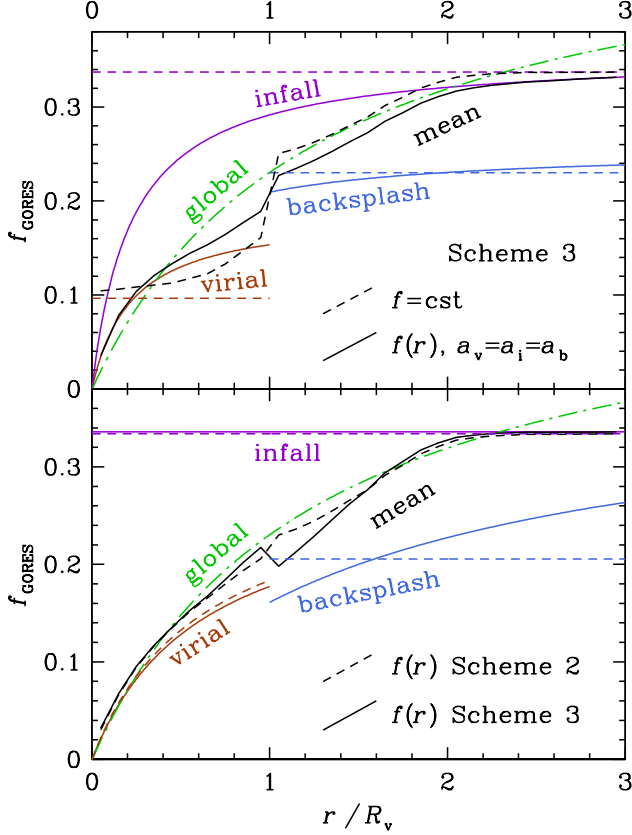


Figure 17. Fraction $f(r)$ of GORES versus physical radius, for the virial (brown), infall (purple) and backplash (blue-grey) populations, their mean (using the cosmological simulation to determine the radial variation of the densities of the three classes, black) and the global deprojection (green dash-dotted curve). *Top:* best fit constant (dashed lines) and radially increasing (Eq. 5) with $a_v = a_i = a_b$ (solid curves), both with Scheme 3. *Bottom:* best fit radially increasing (Eq. 5) with free star formation quenching radii for Schemes 2 (dashed) and 3 (solid curves).

Table 5. Quenching at $r = R_v$ (models with free quenching radii)

Scheme	$f_{\text{GOES}}^{\text{vir}}(R_v)$	$f_{\text{GOES}}^{\text{inf}}(R_v)$	$f_{\text{GOES}}^{\text{bsp}}(R_v)$	quenching
0	0.22	0.28	0.17	1.7
1	0.19	0.34	0.16	1.3
2	0.18	0.33	0.21	0.9
3	0.18	0.34	0.16	1.1
4	0.17	0.24	0.28	-0.7
5	0.18	0.30	0.27	0.2

Note: the last column lists $Q = (f_{\text{GOES}}^{\text{inf}} - f_{\text{GOES}}^{\text{bsp}})/(f_{\text{GOES}}^{\text{inf}} - f_{\text{GOES}}^{\text{vir}})$, which measures the effectiveness of quenching of the backplash population relative to the infall and virial ones. The best fitting scheme 3 is highlighted in bold.

between those of the infalling and virialised populations, although closer to the virialised one (top panel of Fig. 17).

Table 5 displays the fraction of GORES at the surface of the virial sphere ($r = R_v$) for the better-fitting radially-varying models with free quenching radii. The backplash quenching factor, $Q = (f_{\text{GOES}}^{\text{inf}} - f_{\text{GOES}}^{\text{bsp}})/(f_{\text{GOES}}^{\text{inf}} - f_{\text{GOES}}^{\text{vir}})$, should lie between 0 (no quenching: backplash and infall have the same

GOES fraction at a given radius) and 1 (full quenching: backplash and virial have same GORES fraction at a given r). The values above unity imply that the fraction of GORES in the backplash population lying on the virial sphere is lower than the corresponding fraction of the virial population at the same location. This leads to the unphysical result that on the virial sphere backplash galaxies are more passive than the virialised ones.

For our best-fitting Scheme 3, $Q = 1.1$ is just above unity, i.e. the backplash and virialised populations on the virial sphere have very similar fractions of GORES⁶, while for the second best fitting Scheme 2, $Q = 0.9$ (see bottom panel of Fig. 17). On the other hand, for Scheme 4, Q is much smaller than 0: the fraction of GORES for galaxies lying on the virial sphere is higher for the backplash galaxies than for the infall population. This again appears to be an unphysical result, which leads us to disregard Scheme 4 (which fits the data worse than Scheme 3, but with only marginal significance; see Table 4). This suggests that *the backplash galaxies are strongly quenched relative to the infalling ones*, at least half the way from infalling to virialised galaxies at $r = R_v$ (for Scheme 5, which is only marginally consistent with the data) to nearly fully quenched to the level of virialised galaxies (Schemes 3 and 2).

In contrast, using hydrodynamical cosmological simulations of the Local Group, Knebe et al. (2011) find that the luminosity function of backplash galaxies is similar to that of the infalling galaxies and that the total mass within the radius containing the outermost stars divided by the luminosity is higher for infalling galaxies than for backplash galaxies. The first result suggests little quenching of star formation as dwarf galaxies cross through the virial sphere of the Milky Way, while the second result suggests inverse quenching, that is that backplash galaxies have higher luminosity per unit mass. However, star formation in $10^{12} M_\odot$ galaxies falling into $10^{14} M_\odot$ clusters should be similar to the quenching of star formation in dwarf galaxies of mass $10^{10} M_\odot$ falling into the Milky Way virial sphere. What is more surprising is that fig. 5 of Knebe et al. (2011) indicates that galaxies in the virialised class have higher luminosity for given internal velocity dispersion than galaxies in the infall class. Analysing the residuals of luminosity versus velocity dispersion relative to the mean global trend, we deduce that the higher luminosity of virialised galaxies compared to infall galaxies of the same velocity dispersion is statistically significant (with 99.9% confidence using a K-S test, and by typically two magnitudes). The backplash population on the other hand is intermediate but not inconsistent with either the virial or the infall populations. The higher luminosities of the virial population of simulated dwarfs appear to contradict the observed positive luminosity – radius correlation found for luminous virialised galaxies with cluster-centric distances above $\gtrsim 0.1 R_v$ from their parent rich clusters (Adami et al. 1998).

The quest for the physical mechanism responsible for this quenching is beyond the scope of this paper, be it tidal stripping, ram pressure stripping, harassment, starvation or pre-processing in groups. For instance, van den Bosch et al. (2008) argue that the lack of dependence of galaxy colour on cluster mass is evidence against the dominance of ram pressure stripping and harassment.

We note that in our two best-fitting models (Schemes 3 and 2), the fraction of GORES in infalling galaxies is independent of their physical distance to the cluster. Our best-fit model requires a scheme (like our Scheme 3) where galaxies within the virial sphere with high outgoing velocities are equivalent to the infalling galax-

⁶ Forcing $Q = 1$ in our fit leads to χ^2_ν only 0.003 higher for Scheme 3.

ies within the same volume (those with strong negative velocities). This together with the comparison of GORES fraction at the virial radius suggest that *the star formation in galaxies is quenched on a timescale comparable to the time taken for a galaxy to bounce out of a cluster and reach its virial radius*. This timescale corresponds to about 1 to 2 Gyr, which is very close to the lookback time to which our joint H δ -D $_n$ 4000 GORES diagnostic is most sensitive (§2.3). Correcting for this lookback time, one concludes that *star formation in a galaxy is nearly fully quenched in a single passage through the cluster*.

Of course, there will be a variety of orbital pericentres for the infalling galaxies, leading to different degrees of quenching. But the typical high elongations found for orbits in Λ CDM simulations (Ghigna et al. 1998) suggests that orbits with large pericentres will be rare.

We find that $17.9 \pm 0.4\%$ ⁷ of the galaxies within the *virial cylinder* (projected radii $R < R_v$ and $|v_{\text{LOS}}| < 3\sigma_v$) are GORES. This can be compared to the fraction of blue galaxies within the virial cylinder: we find that $20.3 \pm 0.4\%$ of the galaxies with $R < R_v$ are 0.2 magnitude bluer than the Red Sequence (this fraction is fairly consistent with the $\sim 78\%$ of SDSS cluster galaxies that Yang et al. 2008 find to lie on the Red Sequence). So, *within the virial cylinder, the fraction of GORES is roughly $88 \pm 0.5\%$ of the fraction of blue galaxies*, although some blue galaxies are not GORES and some GORES are not blue (Mahajan & Raychaudhury 2009).

In comparison, using the same cosmological simulation as in the present article, Mamon et al. (2010) recently showed that $23 \pm 1\%$ of galaxies within the virial cylinder are outside the virial sphere. As discussed by Mamon et al., the match between fraction of blue galaxies and fraction of cluster interlopers is probably a coincidence since some galaxies within the cluster sphere must be blue and some interlopers must be Red Sequence galaxies in projected groups.

With our models, we can estimate the fraction of GORES within the *virial sphere* using the average of the mean fractions $f(r)$ (Fig. 17) weighted by r^2 times the galaxy number density profile, $\nu(r)$ measured in our cosmological simulation. Results given in Table 6 indicate that for our three best-fitting models (see Table 4), *the fraction of GORES within the virial sphere is $13 \pm 1\%$* . We then predict the fraction of blue galaxies within the virial sphere to be $13/0.88 = 15 \pm 2\%$.

Now, while most galaxies within the virial sphere are part of the virial population, some are infalling (Schemes 1 to 3) or back-splash (Scheme 2). Yet, we can proceed even further and estimate the fraction of GORES among the virialised class, again using our cosmological simulation to perform the calibration. As seen in Table 6, *the fraction of GORES among the virialised class is not zero, but typically $11 \pm 1\%$* . We also predict that the fraction of blue galaxies among the virialised population is $11/0.88 = 12.5 \pm 2\%$. Moreover, Table 6 indicates that the fraction of GORES among the $R < 2R_v$ infall galaxies is $34 \pm 1\%$ while among the back-splash galaxies the fraction of GORES is typically $20 \pm 4\%$ (for Schemes 3, 2 and 1) or perhaps as high as $27 \pm 4\%$ (Schemes 4 and 5).

The presence of GORES among the virialised class might be caused by those low metallicity galaxies for which our H δ -D $_n$ 4000 estimator of recent efficient star formation has a lookback time as

Table 6. Fractions of Galaxies with Ongoing or Recent Efficient Star Formation

Model	Scheme	Virial cylinder $R < R_v$	Virial sphere $r < R_v$	Virial class $(r < R_v)$	Infall class $R < 2R_v$	Backsplash class $R < 2R_v$
Range						
$f=\text{cst}$	3	0.17	0.12	0.10	0.34	0.23
$a_v=a_i=a_b$	3	0.17	0.13	0.11	0.33	0.22
$f(r)$	1	0.17	0.13	0.12	0.34	0.19
$f(r)$	2	0.17	0.13	0.11	0.33	0.21
$f(r)$	3	0.17	0.13	0.11	0.34	0.19
$f(r)$	4	0.17	0.13	0.11	0.32	0.26
$f(r)$	5	0.17	0.13	0.11	0.34	0.27
SDSS	—	0.176	—	—	—	—

Notes: The last six models are our best-fitting ones ($\chi^2_\nu \leq 1.6$). The best fitting scheme 3 is highlighted in bold. Note that the fractions of GORES within the virial cylinder slightly underestimate the observed fraction, but are consistent with it within the 1% errors.

long as 3 Gyr (§2.3). Alternatively, these GORES might be the consequence of star formation triggered by rapid flybys and rare ongoing direct (satellite-satellite) mergers in clusters.

Finally, our statistics lead us to conclude that a fraction $0.13 \times (1 - 0.23)/0.18 = 0.56$ of the GORES within the virial cylinder are within the virial sphere, so that *$44 \pm 2\%$ of GORES within the virial cylinder are outside the virial sphere*, for all good-fitting Schemes.

Note that the asymptotic behaviour of the best-fitt models disagrees with the field value by at least 10%. One may think that this discrepancy may be due to a different set of environment-dependent phenomenon become efficient in modulating galaxy properties at $R > 2R_v$ from the centres of clusters, or to the oversimplified models we used to deproject the fraction of GORES. However, according to the cosmological simulation we analysed here, the high absolute LOS velocity galaxies at $R > R_v$ ought to lie at similar very far distances from the cluster centres (12 virial radii, see Fig. 15) as the field galaxies. Therefore, the discontinuity in the observed fraction of GORES between these galaxies and the field is puzzling and remains an open question.

5.5 Epilogue

In summary, our work shows that the galaxy properties in and around clusters are not simple functions of stellar mass and local environment (e.g. Haines et al. 2007; von der Linden et al. 2010), but also of absolute LOS velocity. With these velocities, it is then statistically feasible to segregate the infalling and back-splash galaxies at any cluster-centric radius, including cluster outskirts. This velocity modulation will be better seen in the properties of the relatively low-mass galaxies, because they are the first ones to be influenced by any changes in their immediate environment (see Mahajan et al. 2011 for such an effect seen in the nearby Coma cluster). It would be worthwhile to extend our analysis using other indicators of very recent star formation to 1) confirm our conclusion that the quenching of star formation occurs in a single passage through the cluster, and 2) assess the fraction of galaxies with very recent star formation among the virialised population. The survival of low-mass galaxies and of star formation in galaxies of all mass, as they pass through the cluster core, lead to important issues that

⁷ The errors here and below on the fractions of GORES are binomial and do not incorporate cosmic variance.

should also be addressed with high-resolution cosmological hydrodynamical simulations.

ACKNOWLEDGEMENTS

SM is supported by grants from ORSAS, UK, and the University of Birmingham. We thank the anonymous referee for useful comments and references. GAM thanks G. Murante for providing the cosmological simulation, and A. Biviano, G. Kauffmann, M. Sarzi, T. J. Ponman, and V. Wild for useful conversations. SM is grateful to B. M. Poggianti for a useful discussion. Funding for the Sloan Digital Sky Survey (SDSS) has been provided by the Alfred P. Sloan Foundation, the Participating Institutions, the National Aeronautics and Space Administration, the National Science Foundation, the U.S. Department of Energy, the Japanese Monbukagakusho, and the Max Planck Society. The SDSS Web site is <http://www.sdss.org/>.

REFERENCES

- Adami C., Biviano A., Mazure A., 1998, *A&A*, 331, 439
- Adelman-McCarthy J. K., the SDSS collaboration, 2006, *ApJS*, 162, 38
- Akaike H., 1974, *IEEE Trans. Automatic Control*, 19, 716
- Balogh M. et al., 2004a, *MNRAS*, 348, 1355
- Balogh M. L., Baldry I. K., Nichol R., Miller C., Bower R., Glazebrook K., 2004b, *ApJ*, 615, L101
- Balogh M. L., Navarro J. F., Morris S. L., 2000, *ApJ*, 540, 113
- Bekki K., 1999, *ApJ*, 510, L15
- Bertschinger E., 1985, *ApJS*, 58, 39
- Biviano A., Girardi M., Giuricin G., Mardirossian F., Mezzetti M., 1992, *ApJ*, 396, 35
- Biviano A., Katgert P., Mazure A., Moles M., den Hartog R., Perea J., Focardi P., 1997, *A&A*, 321, 84
- Blanton M. R. et al., 2003, *ApJ*, 592, 819
- Blanton M. R. et al., 2005, *AJ*, 129, 2562
- Borgani S. et al., 2004, *MNRAS*, 348, 1078
- Bothun G. D., Schombert J. M., 1990, *ApJ*, 360, 436
- Brinchmann J., Charlot S., White S. D. M., Tremonti C., Kauffmann G., Heckman T., Brinkmann J., 2004, *MNRAS*, 351, 1151
- Bruzual G., A., Charlot S., 1993, *ApJ*, 405, 538
- Charlot S., Fall S. M., 2000, *ApJ*, 539, 718
- Charlot S., Longhetti M., 2001, *MNRAS*, 323, 887
- Chincarini G., Rood H. J., 1977, *ApJ*, 214, 351
- Damen M., Labbé I., Franx M., van Dokkum P. G., Taylor E. N., Gawiser E. J., 2009, *ApJ*, 690, 937
- de Vaucouleurs G., 1961, *ApJS*, 6, 213
- Dressler A., 1980, *ApJ*, 236, 351
- Ghigna S., Moore B., Governato F., Lake G., Quinn T., Stadel J., 1998, *MNRAS*, 300, 146
- Gill S. P. D., Knebe A., Gibson B. K., 2005, *MNRAS*, 356, 1327
- Girardi M., Rigoni E., Mardirossian F., Mezzetti M., 2003, *A&A*, 406, 403
- Gnedin O. Y., Hernquist L., Ostriker J. P., 1999, *ApJ*, 514, 109
- Gunn J. E., Gott J. R., 1972, *ApJ*, 176, 1
- Haines C. P., Gargiulo A., La Barbera F., Mercurio A., Merluzzi P., Busarello G., 2007, *MNRAS*, 381, 7
- Haines C. P., La Barbera F., Mercurio A., Merluzzi P., Busarello G., 2006, *ApJ*, 647, L21
- Helou G., Salpeter E. E., Krumm N., 1979, *ApJ*, 228, L1
- Hurvich C. M., Tsai C.-L., 1989, *Biometrika*, 76, 297
- Jiang C. Y., Jing Y. P., Faltenbacher A., Lin W. P., Li C., 2008, *ApJ*, 675, 1095
- Kauffmann G. et al., 2003, *MNRAS*, 341, 33
- Klimontowski J., Łokas E. L., Kazantzidis S., Mayer L., Mamon G. A., 2009, *MNRAS*, 397, 2015
- Knebe A., Libeskind N. I., Knollmann S. R., Martinez-Vaquero L. A., Yepes G., Gottlöber S., Hoffman Y., 2011, *MNRAS*, 412, 529
- Larson R. B., Tinsley B. M., Caldwell C. N., 1980, *ApJ*, 237, 692
- Łokas E. L., Kazantzidis S., Majewski S. R., Law D. R., Mayer L., Frinchaboy P. M., 2010, *ApJ*, 725, 1516
- Mahajan S., Haines C. P., Raychaudhury S., 2010, *MNRAS*, 404, 1745
- Mahajan S., Haines C. P., Raychaudhury S., 2011, *MNRAS*, 412, 1098
- Mahajan S., Raychaudhury S., 2009, *MNRAS*, 400, 687
- Mahajan S., Raychaudhury S., Pimblet K. B., 2011, *MNRAS*, to be submitted
- Mamon G. A., 1992, *ApJ*, 401, L3
- Mamon G. A., Biviano A., Murante G., 2010, *A&A*, 520, A30
- Mamon G. A., Parker Q. A., Proust D., 2001, *Publications of the Astronomical Society of Australia*, 18, 232
- Mamon G. A., Sanchis T., Salvador-Solé E., Solanes J. M., 2004, *A&A*, 414, 445
- Mauduit J.-C., Mamon G. A., 2007, *A&A*, 475, 169
- Merritt D., 1983, *ApJ*, 264, 24
- Mohr J. J., Geller M. J., Fabricant D. G., Wegner G., Thorstensen J., Richstone D. O., 1996, *ApJ*, 470, 724
- Moore B., Katz N., Lake G., Dressler A., Oemler A., 1996, *Nat*, 379, 613
- Moss C., Dickens R. J., 1977, *MNRAS*, 178, 701
- Natarajan P., Kneib J., Smail I., Treu T., Ellis R., Moran S., Limousin M., Czoske O., 2009, *ApJ*, 693, 970
- Navarro J. F., Frenk C. S., White S. D. M., 1996, *ApJ*, 462, 563
- Noeske K. G. et al., 2007a, *ApJ*, 660, L47
- Noeske K. G. et al., 2007b, *ApJ*, 660, L43
- Oemler A., Dressler A., Kelson D., Rigby J., Poggianti B. M., Fritz J., Morrison G., Smail I., 2009, *ApJ*, 693, 152
- Pimblet K. A., 2011, *MNRAS*, 411, 2637
- Pimblet K. A., Smail I., Edge A. C., O'Hely E., Couch W. J., Zabludoff A. I., 2006, *MNRAS*, 366, 645
- Porter S. C., Raychaudhury S., 2007, *MNRAS*, 375, 1409
- Porter S. C., Raychaudhury S., Pimblet K. A., Drinkwater M. J., 2008, *MNRAS*, 388, 1152
- Rines K., Geller M. J., Kurtz M. J., Diaferio A., 2003, *AJ*, 126, 2152
- Rines K., Geller M. J., Kurtz M. J., Diaferio A., 2005, *AJ*, 130, 1482
- Sanchis T., Łokas E. L., Mamon G. A., 2004, *MNRAS*, 347, 1198
- Sandage A., Tammann G. A., 1976, *ApJ*, 210, 7
- Saro A., Borgani S., Tornatore L., Dolag K., Murante G., Biviano A., Calura F., Charlot S., 2006, *MNRAS*, 373, 397
- Sodre L., Jr., Capelato H. V., Steiner J. E., Mazure A., 1989, *AJ*, 97, 1279
- Struble M. F., 1979, *AJ*, 84, 27
- van den Bosch F. C., Aquino D., Yang X., Mo H. J., Pasquali A., McIntosh D. H., Weinmann S. M., Kang X., 2008, *MNRAS*, 387, 79
- Vollmer B., 2009, *A&A*, 502, 427
- von der Linden A., Wild V., Kauffmann G., White S. D. M., Weinmann S., 2010, *MNRAS*, 404, 1231

- Worthey G., Ottaviani D. L., 1997, ApJS, 111, 377
Yang X., Mo H. J., van den Bosch F. C., 2008, ApJ, 676, 248
Yang X., Mo H. J., van den Bosch F. C., 2009, ApJ, 695, 900
Yang X., Mo H. J., van den Bosch F. C., Pasquali A., Li C., Barden
M., 2007, ApJ, 671, 153

Table A1. K-S test probabilities for the null hypothesis that pairs of subsamples have distributions of M^* arising from the same parent distribution. Columns $v1$, $v2$, and $v3$ correspond to $|v_{\text{LOS}}|/\sigma_v = 0-1$, $1-2$, and $2-3$, respectively. Statistically significant differences between subsample pairs are highlighted in bold.

	$R/R_v \leq 0.5$			$0.5 < R/R_v \leq 1.0$			$1.0 < R/R_v \leq 1.5$			$1.5 < R/R_v \leq 2.0$			field
	$v1$	$v2$	$v3$	$v1$	$v2$	$v3$	$v1$	$v2$	$v3$	$v1$	$v2$	$v3$	
	1	2	3	4	5	6	7	8	9	10	11	12	
1	1.0E+00	7.3E-08	2.5E-09	4.2E-20	2.9E-20	1.6E-09	1.2E-12	1.8E-09	4.1E-08	2.7E-11	1.4E-10	8.5E-06	0.0E+00
2		1.0E+00	1.7E-02	3.1E-03	6.2E-06	9.9E-04	5.9E-03	6.1E-02	1.2E-03	2.1E-02	5.5E-02	6.5E-02	2.6E-13
3			1.0E+00	1.7E-01	3.6E-01	3.6E-01	4.3E-02	1.2E-01	2.6E-01	3.6E-02	3.2E-01	7.3E-01	2.6E-01
4				1.0E+00	2.8E-02	1.3E-01	2.1E-01	7.6E-01	2.3E-01	1.4E-01	8.8E-01	6.7E-01	5.6E-07
5					1.0E+00	6.5E-01	2.5E-02	8.8E-01	8.9E-01	3.3E-03	3.2E-02	6.4E-01	1.3E-01
6						1.0E+00	3.8E-02	9.9E-02	7.8E-01	2.0E-02	7.9E-02	2.6E-01	1.8E-01
7							1.0E+00	7.9E-01	1.0E-01	9.7E-01	5.8E-01	6.7E-01	2.6E-04
8								1.0E+00	1.5E-01	8.4E-01	7.9E-01	8.3E-01	5.4E-03
9									1.0E+00	4.3E-02	9.9E-02	5.2E-01	4.3E-01
10										1.0E+00	4.9E-01	7.0E-01	5.4E-06
11											1.0E+00	9.1E-01	3.7E-03
12												1.0E+00	3.8E-01

Table A2. Same as Table A1, but with BCGs excluded.

	$R/R_v \leq 0.5$			$0.5 < R/R_v \leq 1.0$			$1.0 < R/R_v \leq 1.5$			$1.5 < R/R_v \leq 2.0$			field
	$v1$	$v2$	$v3$	$v1$	$v2$	$v3$	$v1$	$v2$	$v3$	$v1$	$v2$	$v3$	
	1	2	3	4	5	6	7	8	9	10	11	12	
1	1.0E+00	5.2E-08	6.6E-10	1.5E-20	1.2E-21	1.2E-09	6.9E-15	9.0E-10	6.5E-09	2.0E-12	9.5E-11	3.9E-06	0.0E+00
2		1.0E+00	9.2E-03	1.5E-03	1.7E-06	2.3E-04	8.9E-04	3.6E-02	5.1E-04	4.0E-03	3.8E-02	3.8E-02	3.9E-13
3			1.0E+00	2.0E-01	4.3E-01	2.7E-01	9.8E-02	1.3E-01	2.5E-01	4.4E-02	2.2E-01	7.4E-01	3.4E-01
4				1.0E+00	2.3E-02	6.3E-02	5.5E-01	7.6E-01	1.7E-01	3.0E-01	8.5E-01	6.5E-01	2.6E-06
5					1.0E+00	6.9E-01	4.6E-02	1.0E-01	8.4E-01	5.4E-03	2.5E-02	6.7E-01	5.8E-01
6						1.0E+00	6.7E-02	7.7E-02	7.3E-01	3.4E-02	4.1E-02	2.6E-01	1.5E-01
7							1.0E+00	9.8E-01	1.0E-01	8.9E-01	8.1E-01	7.8E-01	4.5E-03
8								1.0E+00	1.3E-01	8.9E-01	7.3E-01	8.7E-01	1.7E-02
9									1.0E+00	5.2E-02	6.9E-02	4.5E-01	1.9E-01
10										1.0E+00	4.9E-01	6.8E-01	5.8E-05
11											1.0E+00	9.0E-01	8.2E-03
12												1.0E+00	5.3E-01

APPENDIX A: KOLMOGOROV-SMIRNOV STATISTICS

In this appendix, we present tables of probabilities, from the Kolmogorov-Smirnov test, that various sub-samples of different physical quantities arise from the same parent distributions (see § 3).

Table A3. Same as Table A1, but for the difference between the $(g-r)^{0.1}$ colour and the best-fitted red sequence (RS).

	$R/R_v \leq 0.5$			$0.5 < R/R_v \leq 1.0$			$1.0 < R/R_v \leq 1.5$			$1.5 < R/R_v \leq 2.0$			field
	$v1$	$v2$	$v3$	$v1$	$v2$	$v3$	$v1$	$v2$	$v3$	$v1$	$v2$	$v3$	
	1	2	3	4	5	6	7	8	9	10	11	12	
1	1.0E+00	1.2E-01	1.0E-04	5.9E-30	3.4E-29	1.3E-10	0.0E+00	0.0E+00	2.0E-29	0.0E+00	0.0E+00	9.0E-27	0.0E+00
2		1.0E+00	1.7E-02	1.5E-16	6.1E-17	1.8E-07	1.0E-41	7.3E-41	6.2E-23	1.4E-45	8.4E-36	7.6E-20	0.0E+00
3			1.0E+00	5.8E-05	4.6E-06	1.6E-02	1.2E-13	4.5E-16	1.8E-12	3.9E-15	2.5E-13	2.4E-08	0.0E+00
4				1.0E+00	5.6E-02	3.3E-01	1.3E-11	1.2E-14	3.8E-10	2.2E-15	2.2E-11	1.1E-07	0.0E+00
5					1.0E+00	8.1E-01	1.1E-04	1.6E-07	1.3E-06	5.4E-06	1.8E-05	1.0E-04	0.0E+00
6						1.0E+00	2.4E-03	4.1E-05	6.1E-05	8.0E-04	9.9E-04	5.5E-03	4.9E-29
7							1.0E+00	1.1E-01	1.8E-02	6.1E-01	2.7E-01	1.0E-01	0.0E+00
8								1.0E+00	3.3E-01	1.3E-01	6.5E-01	3.6E-01	1.7E-23
9									1.0E+00	5.0E-02	1.5E-01	1.5E-01	3.0E-06
10										1.0E+00	8.1E-01	4.8E-01	0.0E+00
11											1.0E+00	5.6E-01	1.4E-31
12												1.0E+00	1.9E-16

Table A4. Same as Table A1, but for SFR/ M^* .

	$R/R_v \leq 0.5$			$0.5 < R/R_v \leq 1.0$			$1.0 < R/R_v \leq 1.5$			$1.5 < R/R_v \leq 2.0$			field
	$v1$	$v2$	$v3$	$v1$	$v2$	$v3$	$v1$	$v2$	$v3$	$v1$	$v2$	$v3$	
	1	2	3	4	5	6	7	8	9	10	11	12	
1	1.0E+00	5.8E-04	1.0E-04	1.0E-26	8.1E-28	4.7E-12	0.0E+00	5.6E-45	1.1E-22	0.0E+00	1.8E-40	1.5E-21	0.0E+00
2		1.0E+00	1.7E-02	1.0E-08	6.2E-13	1.3E-06	4.1E-25	1.1E-25	1.2E-16	2.1E-33	1.7E-21	1.2E-14	0.0E+00
3			1.0E+00	3.4E-03	1.4E-02	3.1E-02	1.5E-06	1.1E-07	7.5E-08	1.0E-07	2.5E-06	3.4E-06	1.6E-21
4				1.0E+00	6.1E-02	8.4E-02	4.1E-07	1.6E-09	4.5E-09	2.3E-11	3.2E-08	7.9E-07	0.0E+00
5					1.0E+00	4.7E-01	6.2E-04	1.1E-04	6.1E-06	3.0E-05	3.4E-04	1.8E-04	1.4E-26
6						1.0E+00	9.1E-03	2.3E-02	6.3E-03	4.1E-03	1.6E-02	1.1E-02	5.5E-07
7							1.0E+00	1.5E-01	2.5E-03	3.0E-01	7.3E-02	2.9E-02	1.9E-17
8								1.0E+00	9.7E-02	4.6E-01	5.2E-01	4.5E-01	2.9E-05
9									1.0E+00	1.7E-02	8.9E-02	7.5E-01	1.1E-01
10										1.0E+00	4.3E-01	1.9E-01	2.7E-14
11											1.0E+00	6.0E-01	1.8E-08
12												1.0E+00	2.9E-03

Table A5. Same as Table A1, but for H δ .

	$R/R_v \leq 0.5$			$0.5 < R/R_v \leq 1.0$			$1.0 < R/R_v \leq 1.5$			$1.5 < R/R_v \leq 2.0$			field
	$v1$	$v2$	$v3$	$v1$	$v2$	$v3$	$v1$	$v2$	$v3$	$v1$	$v2$	$v3$	
	1	2	3	4	5	6	7	8	9	10	11	12	
1	1.0E+00	1.7E-06	7.0E-09	0.0E+00	0.0E+00	6.1E-22	0.0E+00	0.0E+00	8.9E-37	0.0E+00	0.0E+00	1.1E-27	0.0E+00
2		1.0E+00	6.6E-04	1.4E-18	2.6E-24	9.6E-14	3.7E-38	7.7E-39	4.4E-25	1.5E-39	6.2E-35	1.6E-17	0.0E+00
3			1.0E+00	6.0E-03	8.5E-05	2.8E-03	7.3E-07	2.8E-10	2.0E-09	2.7E-06	9.4E-08	1.2E-04	4.4E-36
4				1.0E+00	2.4E-03	5.8E-03	7.2E-07	1.9E-11	4.4E-11	1.3E-08	3.6E-09	1.4E-04	0.0E+00
5					1.0E+00	7.8E-01	2.0E-01	2.4E-04	2.7E-06	5.5E-02	1.3E-02	7.8E-02	1.6E-42
6						1.0E+00	2.1E-01	1.6E-02	6.4E-04	2.2E-01	7.7E-02	1.7E-01	1.0E-12
7							1.0E+00	3.6E-02	3.6E-04	1.0E-01	3.1E-01	5.7E-01	6.1E-42
8								1.0E+00	1.6E-01	1.8E-02	3.2E-01	4.3E-01	5.4E-13
9									1.0E+00	9.9E-04	1.0E-02	6.6E-02	1.3E-02
10										1.0E+00	4.1E-01	8.6E-01	1.0E-43
11											1.0E+00	9.8E-01	9.1E-19
12												1.0E+00	7.3E-09

Table A6. Same as Table A1, but for D_n4000 .

	$R/R_v \leq 0.5$			$0.5 < R/R_v \leq 1.0$			$1.0 < R/R_v \leq 1.5$			$1.5 < R/R_v \leq 2.0$			field
	$v1$	$v2$	$v3$	$v1$	$v2$	$v3$	$v1$	$v2$	$v3$	$v1$	$v2$	$v3$	
	1	2	3	4	5	6	7	8	9	10	11	12	
1	1.0E+00	3.5E-09	5.1E-09	0.0E+00	0.0E+00	9.8E-15	0.0E+00	0.0E+00	8.8E-35	0.0E+00	0.0E+00	1.2E-27	0.0E+00
2		1.0E+00	1.1E-04	3.1E-23	1.9E-23	8.4E-09	4.7E-40	6.2E-38	1.9E-24	1.4E-45	1.3E-35	5.2E-18	0.0E+00
3			1.0E+00	8.1E-03	7.2E-05	4.7E-02	7.4E-07	9.2E-09	5.7E-09	9.0E-07	3.7E-08	8.2E-05	1.2E-34
4				1.0E+00	2.2E-02	1.0E-01	1.2E-06	4.8E-09	2.5E-07	1.6E-11	5.6E-09	1.9E-05	0.0E+00
5					1.0E+00	2.8E-01	6.3E-02	8.2E-04	9.8E-05	1.0E-03	5.8E-03	1.7E-02	0.0E+00
6						1.0E+00	1.4E-02	5.6E-04	5.1E-05	1.7E-02	5.2E-03	9.5E-02	1.1E-17
7							1.0E+00	7.1E-02	7.5E-03	1.1E-01	6.9E-02	1.8E-01	0.0E+00
8								1.0E+00	2.1E-01	1.2E-01	9.4E-01	1.0E-01	7.4E-17
9									1.0E+00	2.1E-02	1.1E-01	4.9E-02	1.3E-03
10										1.0E+00	3.5E-01	5.9E-01	2.5E-38
11											1.0E+00	1.2E-01	1.5E-21
12												1.0E+00	4.1E-10